UNIVERSITY OF COPENHAGEN

FACULTY OF SCIENCE

Master Thesis - 3+5 PhD Part A

Cecilie Hede

Evolution of the Rate of SNe IIn with Redshift

Supervisors: Jens Hjorth, Radoslaw Wojtak & Christa Gall

Handed in: September 1, 2021

1 Abstract

The current estimations of the number of lensed supernovae (SNe) IIn expected to be detected with the Vera C. Rubin, Legacy Survey of Time and Space (LSST) could be underestimated, because the results are based on the assumption that the ratio between the number of SNe IIn and the total number of core collapse SNe is independent host galaxy stellar mass. In this thesis, using Lick Observatory Supernova Search (LOSS) data from Graur et al. (2017b), this ratio is instead described using a power law and compared to the constant model, as the data implies a bias for SNe IIn toward low-mass host galaxies. The local ratio is estimated to be 0.034 ± 0.009 using constraints from the LOSS data requiring a constant model, which is not consistent with formerly used values. The calculated volumetric SNe IIn rate is affected by the power law models for a redshift of around 4 and above. In this range the total SNe IIn rate predicts more SNe IIn than the constant model, as the contribution from the least massive galaxies is increased the most. This means that the estimated number of lensed SNe IIn for LSST from Wojtak et al. (2019) are not influenced, since LSST cannot detect lensed SNe above a redshift around 3 as they are too faint.

Contents

2 Introduction

According to the currently accepted cosmological paradigm, the Universe came into existence 13.7 billion years ago in the Big Bang along with the matter that we see around us today, from quarks to protons and neutrons to atomic nuclei to the first atoms of hydrogen and helium. The Universe expanded and cooled down, and matter clumped together to produce gas clouds that collapsed to form the first stars and planets, and eventually the galaxies and clusters observed today, as illustrated in Figure 1. Heavier elements were and are still created in the center of stars and spread across great distances by supernovae (SNe), the collapse of massive stars, in spectacular explosions outshining even the galaxies hosting them. Massive objects like stars, galaxies and clusters distort spacetime around them, such that they have the potential to act as a lens for light from other objects such as SNe. Lensed SNe, as we will see in Section 3, can be used to estimate the current expansion rate of the Universe in an independent way.

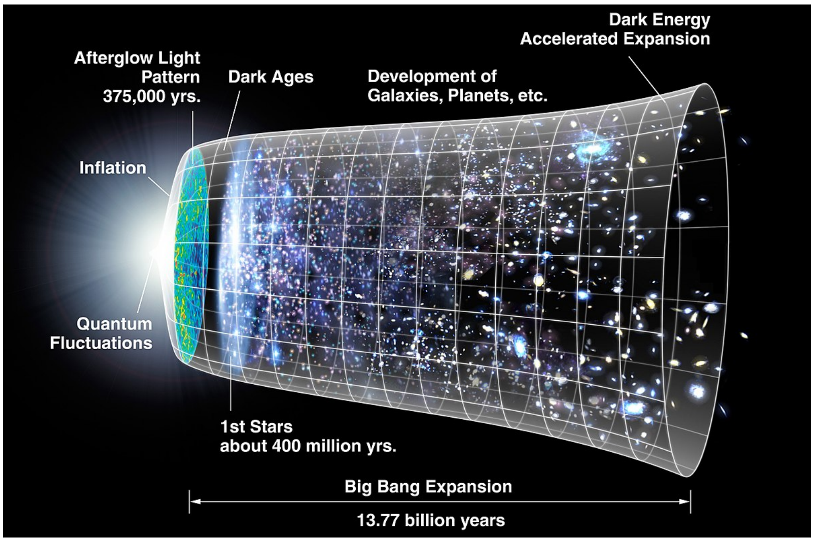

Figure 1: Schematic timeline of the evolution of the Universe since the Big Bang. Credit: NASA/WMAP Science Team.

2.1 Lensed Supernovae IIn

The first lensed SNe (both core-collapse (CC) and Ia) have been observed only some few years ago (Kelly et al., 2015), but have already emerged as useful probes in complementing time-delay cosmography using lensed quasars (e.g. Bonvin et al., 2017), because of their stronger luminosity peaks and shorter time-scales, making time-delay measurements simple and more accurate

(Sanders et al., 2015). The time delays between images, occurring because of the different light paths through expanding space and the gravitational potential, can be used to probe different cosmological parameters such as the Hubble constant H_0 and the spatial curvature density Ω_κ (Linder, 2011).

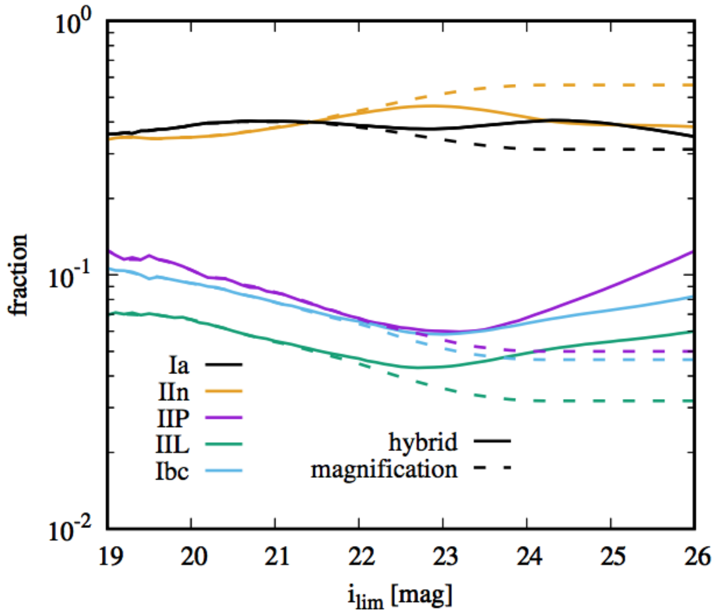

Figure 2: Fractions of five supernova types in samples of gravitationally lensed supernovae for surveys with limiting magnitude i_{lim} in the i-band. Figure taken from Wojtak et al. (2019).

Wojtak et al. (2019) find through simulations that surveys detecting lensed supernovae will be dominated by SNe Ia and SNe IIn. Figure 2 shows that these two types make up about a third of the total lensed supernovae each. In Figure 3, the estimated annual numbers of discovered lensed supernovae are shown for different supernova types in multiple surveys. For current transient surveys like Zwicky Transient Facility (ZTF) and a hypothetical Pan-STARRS survey, the numbers are few and comparable between the different SN types, but the predictions for the Legacy Survey of Space and Time (LSST) from the Vera C. Rubin Observatory are 1 order of magnitude larger, where the dominance of the SNe IIn is immediately apparent.

LSST is an upcoming transient survey with a planned operation period of 10 years using the Vera C. Rubin Telescope, covering about half of the sky. One of the science goals of this survey is to explore the transient optical sky, investigating the nature of many different astrophysical objects such as lensed SNe. LSST will go deeper compared to current and former surveys, which is the main explanation for the larger numbers of expected lensed SNe. The Vera C. Rubin Observatory

survey/detection method	effective area	Type Ia	Type IIP	Type IIL	Type Ib/c	Type IIn
ZTF/magnification	15 000 $\deg^2$	2.1 (r)	0.37 (r)	0.23 (r)	0.36 (r)	3.8 (r)
Pan-STARRS/magnification	3000 $\deg^2$	0.9 (i)	0.20 (i)	0.13 (i)	0.20 (i)	0.8 (i)
LSST/magnification	20 000 $\deg^2$	61(z)	12.2 (z)	8.7 (y)	12.3 (y)	184 (g)
LSST/image multiplicity	20 000 $\deg^2$	44 (i)	6.1 (i)	5.5 (i)	6.8 (i)	88 (g)
LSST/hybrid	20 000 $\deg^2$	89 (iz)	16.3 (iz)	11.9 (iy)	15.8 (iy)	210 (g)

Figure 3: Expected annual numbers of lensed supernovae in different surveys. Table is from Wojtak et al. (2019).

is planned to start full science operations in 2023. The numbers in Figure 3 for LSST are based on different detection strategies like magnification, image multiplicity and a hybrid method of the two yielding the most lensed SNe.

Other estimates of lensed SNe from LSST are from Goldstein et al. (2019), their predictions shown in Figure 4. Again, it is clear that the SNe IIn will dominate for LSST, with similar numbers to what is predicted in Wojtak et al. (2019). In Figure 4, the LSST predictions are based on either `minion_1016` or `altsched`, two leading candidate observing strategies proposed for the upcoming survey.

SN Type	ZTF	LSST (`minion_1016`)	LSST (`altsched`)
Type Ia	1.23	47.84	47.42
Type IIP	2.76	88.51	91.06
Type IIn[a]	3.75	209.31	166.54
Type IIL	0.31	11.69	13.10
Type Ib/c	0.36	14.00	16.15
SN 1991bg-like	0.02	0.79	0.89
SN 1991T-like	0.17	5.41	6.09
Total[a]	8.60	380.60	341.27

[a]Lower limit.

Figure 4: Estimated annual discovery rates of lensed SNe for ZTF and LSST for different SN types. Table is from Goldstein et al. (2019).

There is a lot of evidence supporting the conclusion that SNe IIn will dominate in samples of lensed supernovae. However, these results are based on the assumption that the SNe IIn to CC SNe ratio is not dependent on redshift or host galaxy mass. This means that the current method used in astrophysics is to take the ratio of SNe IIn or any type of CC SNe to the total number of CC SNe found in the local Universe and expand this to apply to all values of redshift. As described in Graur et al. (2015), the volumetric rate of CC SNe is calculated for a median redshift of 0.075 from SNe II rates per unit mass and an assumption that the IIP/L SN subtypes always comprise 60 % of all CC SNe, but does it really make sense that the fraction of IIP/L is always 0.6 no matter the redshift?

Research implies that different SN types have different progenitors to give rise to the light curves characterizing each subtype (Arcavi, 2017). These progenitors in turn have different preferences for host galaxies and their properties. This means that the assumption that the fractions of CC SNe do not change with redshift is not very solid.

For SNe IIn, there could be a bias towards low mass host galaxies for the Lick Observatory Supernova Search data and rates from Graur et al. (2017b), resulting in the numbers from Goldstein et al. (2019) and Wojtak et al. (2019) possibly being underestimated, which constitutes the essence of the research carried out in this thesis. Increased numbers of lensed supernovae, both magnified and multiply-imaged, with the next generation of telescopes like LSST will consequently result in more precise constraints on the cosmological parameters.

This thesis will include background information (Section 3) and description of the data utilized in this thesis (Section 4). In Section 5, power law models are proposed to describe the ratio between SNe IIn and CC SNe as a function of host galaxy stellar mass, and the IIn rates are calculated using these models. In Section 6, the results are discussed and the impact on lensed SNe numbers are investigated using the simulation from Wojtak et al. (2019). Section 7 includes the conclusion and Section 8 outlines some suggestions for future work and extension of this project.

3 Background

The most massive stars in the galaxy will end their lives in a violent and explosive way. Stars with a mass above 8 $M_\odot$ will evolve into what we call a supernova. As the fusion in the core uses up first hydrogen, then helium and other elements all the way to iron, the electron degeneracy pressure is not sufficient to withstand the force of gravity and the core consequently collapses. This is why we call them core-collapse SNe. For SNe Ia however, it is a different story. The mechanisms behind these SNe are still subjects of active research but the two most popular theories are the single- and double-degenerate scenarios, where there are two stars in a binary, either two carbon-oxygen white dwarfs (CO WD) or one CO WD and a main sequence star. The primary star accretes mass from the secondary, which triggers the SN explosion, when the core of the CO WD reaches the Chandrasekhar mass of $1.37 M_\odot$. This means that theoretically SNe Ia should have almost the same absolute luminosity and so can be used as standard candles to determine distances in the Universe (Meng et al., 2017; Maguire, 2017). In this thesis, I will study primarily the CC SNe, with a particular focus on SNe IIn.

3.1 Supernova Types

The CC category is split into many different types of SNe as can be seen in Figure 5.

The CC category covers all except Ia and are split into hydrogen-rich and hydrogen-poor, with this dichotomy constituting the difference between type II and I. Type II all have different hydrogen and lightcurve characteristics, which is how we have chosen to divide them into different categories. The difference between type IIP and IIL, for example, can be found in their lightcurves, where IIP has a characteristic plateau whereas IIL decreases linearly. It is speculated that the reason behind this diversity in hydrogen-rich SNe can be due to differences in progenitor mass, rotation and binarity among other factors (Arcavi, 2017).

3.1.1 SNe IIn

The rationale behind the classification of type IIn is the presence of narrow hydrogen lines in the spectra as noted in Figure 5. The SNe IIn are special in the sense that they are not really a type the same way as other CC SNe. SNe IIn are interactive SNe, which means that what we observe for a IIn is not the SN as for other types but the interaction with the circumstellar material (CSM)

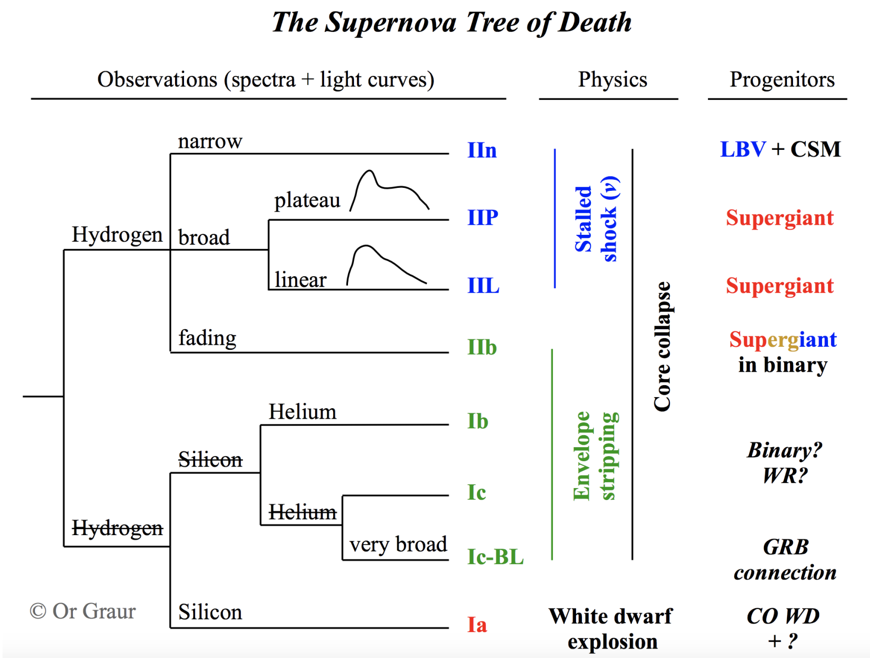

Figure 5: Or Graur's SN tree of death, where LBV, CSM, WR and GRB implies luminous blue variable, circumstellar material, Wolf-Rayet and gamma-ray burst, respectively.

present. The CSM is also what gives rise to the narrow hydrogen lines.

Figure 6 provides a simple overview of the structure of a IIn, dividing the explosion into 4 different zones. Zone 1 is the still unshocked CSM, zone 2 is the CSM that has been swept up by the forward shock from the explosion, zone 3 is SN ejecta that has been decelerated by the reverse shock, and finally, zone 4 is the freely expanding ejecta from the SN. Usually, i.e., for non-interactive SNe, we only observe what is happening in zone 4, where we expect to see broad emission and absorption lines. In between zones 2 and 3 lie the cold dense shell (CDS). This is the area between the shocked CSM and the shocked ejecta from the SN, where material from the two zones mix and cool down. It is speculated that this CDS mechanism could be responsible for the creation of large amounts of the dust that we observe in the Universe (Gall et al., 2014; Bevan et al., 2019). What is shown in Figure 6 is a spherically symmetric CSM, which is of course a simple case and rarely observed in practice. In the case of asymmetric CSM, the situation is more complicated since any of the four zones could be seen simultaneously and spectral features might or might not be seen depending on the viewing angle, which is important to keep in mind for analysis and interpretation of IIn data.

The SNe IIn are in general brighter than other SN types because of the CSM interaction and the radiative shock. The brightness of the SN essentially depends on the mass loss rate of the pro-

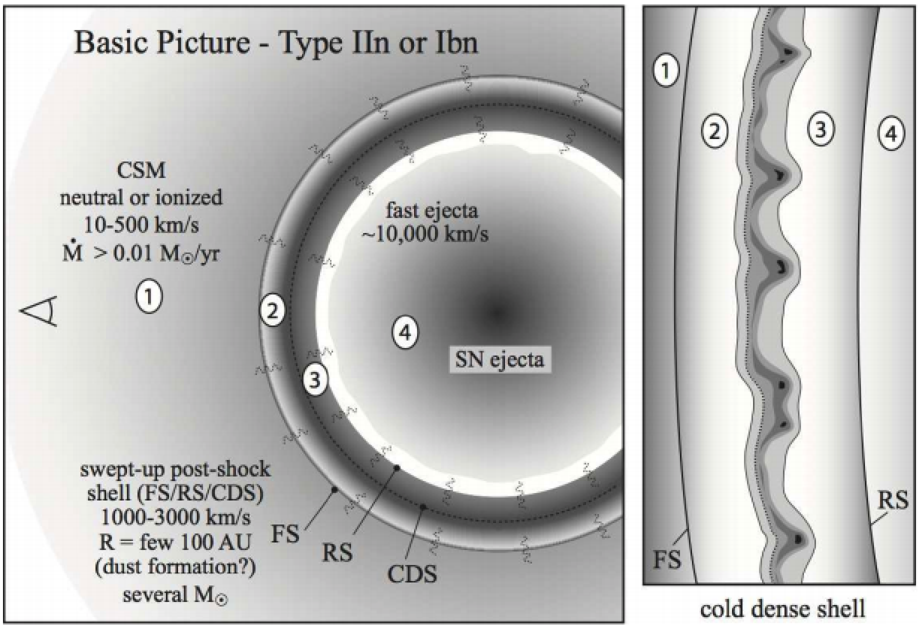

Figure 6: Schematic representation of a type IIn SN from Smith (2017).

genitor, and this value can be estimated to be of order 0.01 $M_{\odot}$/yr for an average type IIn (Smith, 2017). This amount of mass loss goes beyond any regular stellar winds and therefore, candidates of already observed stellar types, such as luminous blue variables (LBV) and possibly extreme red super giants (RSG) and yellow hyper giants (YHG), have been proposed as progenitors due to their sizes and their recurring mass loss events. These types of stars undergo intervals of mass loss from a period of months (LBV) to thousands of years (YHG), which is necessary to produce the amount of CSM needed for a type IIn SN.

In Figure 7, we see a plot of the mass loss rate against the expansion speed and typical areas for massive stars as well as examples of SNe in black crosses. The plot suggests that the most likely progenitors of interacting SNe are LBVs that have experienced giant eruptions to create a huge amount of CSM. Luminous blue variables are a specific class of very massive stars that show variations, both spectroscopic and photometric, with time. They are also characterized by strong stellar wind mass loss and even giant eruptions explaining the CSM found in a IIn. So far, no massive star evolution model can explain the mechanism behind either the variability or the mass loss of these giant stars (Grassitelli et al., 2020).

The periods of mass loss and/or giants eruptions are large enough to compare to a SN and have sometimes been classified as such. These are known as SN impostors. The latter can look like a IIn with narrow hydrogen lines but are fainter and slower. An example of such an impostor could be

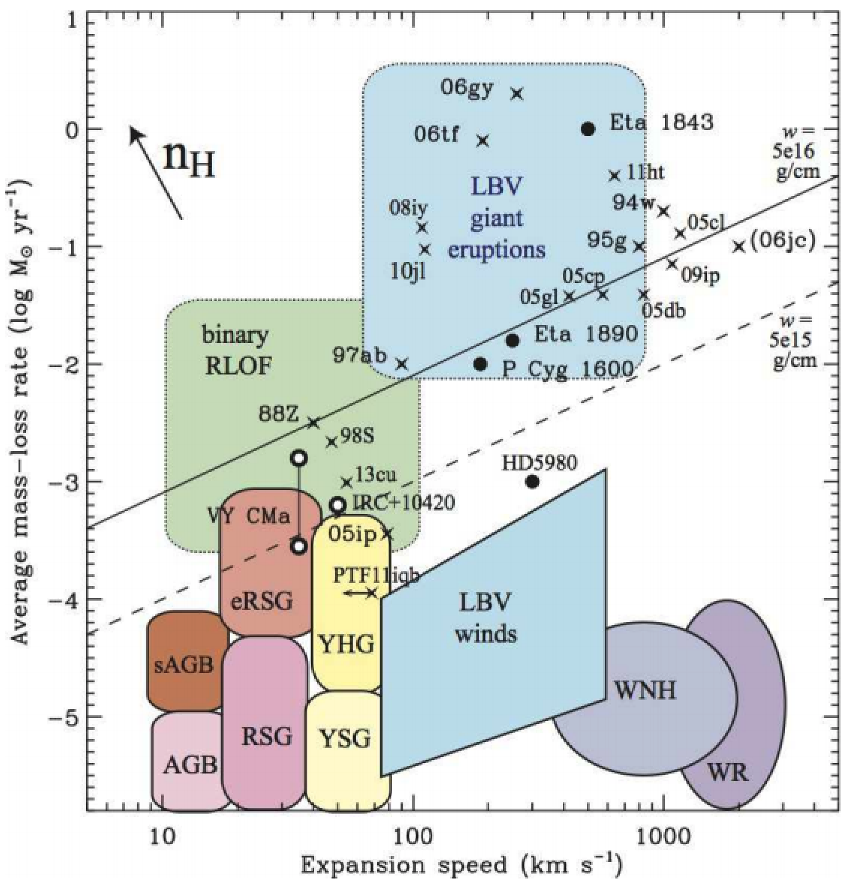

Figure 7: Average mass loss versus expansion speed. The typical areas for different massive stellar types are marked. Figure from Smith (2017).

SN2006jc (classified as a peculiar Ib though with He-rich CSM). This supernova also "exploded" two years before, in 2004, and at that time was thought to be an actual SN. In 2006, it went off again and this time it was believed to be a proper SN explosion and not an impostor. Analysis has shown that the star in 2004 was probably a LBV undergoing an eruption, which could explain the CSM, and that soon after it transitioned to a Wolf-Rayet star before going SN (Foley et al., 2007). For more details on type IIn SNe, we refer the interested reader to Smith (2017).

SNe IIn can be divided into subtypes of either 1988Z-like or 1994W-like. The former on a luminosity scale of -17 to -19 mag in V-band, are believed to be the result of a highly asymmetric CSM interacting with X-ray emission from the SN explosion. This can power the SN for years. The latter, landing at a luminosity of around -18 mag in V-band, exhibits a 100 day plateau in their light curves before a sharp drop in luminosity. Many other less clear cut SNe IIn have been observed over time, making SNe IIn one of the most diverse types of CC SNe. See Stritzinger et al. (2012) for more information.

New research suggests that SNe IIn can be further divided into subcategories of slow and fast risers as well as slow and fast decliners. However, the latter has weaker statistical significance. This is based on a study of 42 SNe IIn from the Palomar Transient Factory (PTF) and intermediate PTF (iPTF) by Nyholm et al. (2020). The typical rise times for SNe IIn are 20 ± 6 d and 50 ± 11 d for fast and slow risers, respectively. For the decline rate, the results are less clear, but a bimodal distribution may exist with slopes of 0.013 ± 0.006 mag per day and 0.040 ± 0.010 mag per day for the initial 50 days after light curve peak. Nyholm et al. (2020) even suggest a new variety of SNe IIn-P, showing a fast rise and a slow linear decline. The SNe IIn-P is a subtype of SNe IIn and is a category that exhibits a sort of plateau behaviour after peak and a fast drop post plateau (Mauerhan et al., 2013). But this proposed new variety by Nyholm et al. (2020) drops much slower than the prototypical IIn-P events. However, the light curve properties of SNe IIn vary greatly within the type due to the nature of the ejecta-CSM interaction, rendering further attempts at classification a challenge.

3.1.2 Superluminous Supernovae

A new class of SNe more luminous and longer-lived than the classical SN types called superluminous supernovae (SLSNe) have been observed and recognized within the last decade or so (Moriya et al., 2018). These very bright transients are separated from the more faint types as they are defined by having an absolute magnitude of less than -21 in optical according to Moriya et al. (2018). SLSNe are also divided into subtypes as the classical SNe. The SLSN-I are hydrogen-poor events, whilst SLSN-II are the hydrogen-rich counterparts. Many of the hydrogen-rich SLSNe exhibit narrow emission lines of the hydrogen Balmer series similar to SNe IIn (Gal-Yam, 2019), and are therefore named SLSN-IIn. It is not clear at this point whether the SLSN-IIn luminosity function (LF) is a smooth extension of the SNe IIn LF or a different population entirely. The definition of the class of SLSNe by a magnitude cut-off is rather arbitrary and not fully established yet. According to a spectroscopic study done by Quimby et al. (2018) on SNe Ibc, Ic-BL and SLSNe-I, there is an apparent threshold of $M_g = -19.8$ mag that separates the fainter events from the more luminous ones. However, this has not been done for the SLSNe-II at this time. The exact mechanism behind SLSNe is as yet not clear, but most SLSNe-II show signs of CSM interaction like SNe IIn which gives an indication that this interaction could power very bright events. Some cases would theoretically require large CSM masses or explosion kinetic energies, but these scenarios are possible explanations for what is observed as SLSN-IIn. See reviews by Moriya et al. (2018) and Gal-Yam (2019) for more details on the current knowledge on SLSNe.

The SNe used in this project are all considered to be regular SNe IIn at this time. However, one is significantly brighter than the rest (SN2010jl; see Table 1 in Section 4.1), but the influence of this fact on the results is not clear due to the lack of understanding of the classical SNe versus SLSNe.

3.1.3 Host Galaxy Mass & Metallicity

Understanding the properties of SN host galaxies and how they are connected to different types of SNe can help us understand the nature of the progenitors and where and when in the Universe we expect to see different subtypes of SNe, both regular and superluminous.

In Kelly & Kirshner (2012), 519 CC SNe host galaxies were analyzed using the properties of color, metallicity and specific star-formation rate. In this case, the metallicity is very interesting, because this can tell us something about the mass of the galaxies as well. According to the mass-metallicity relation (MZR), the metallicity of a galaxy increases with stellar mass, while the fundamental metallicity relation (FMR) suggests that galaxies with higher SFRs have lower metallicity at a fixed stellar mass (Gao et al., 2018). This is useful as we can compare the host galaxy metallicities for different SN subtypes. Kelly & Kirshner (2012) have examined host galaxy populations for all subtypes of CC SNe individually and find for e.g. SNe Ib in metal-rich galaxies and both SNe Ic-BL and IIb in more metal-poor environments compared to Ib, which according to the MZR means more massive host galaxies for Ib than Ic-BL and IIb. For IIn however, the study finds no statistically significant difference for the environments of SNe IIn compared to SNe II. This is not consistent with the study by Graur et al. (2017b), the results of which can be seen in Figure 12, where we see an increasing fraction of SNe IIn with lower host galaxy mass cut-offs. The uncertainties in both studies are substantial and as such, it is not possible to make any definitive conclusions on the SNe IIn host galaxies and their mass based on these results. The analysis in this thesis is based on the results from Graur et al. (2017b).

The first systematic study of the host galaxies of SLSNe was done by Neill et al. (2011) and shows that hosts are typically low-mass galaxies with a high specific star-formation rate, but these results are very limited by the depth of the observations. More recent research, such as Angus et al. (2016) which included 21 SLSN hosts, and Schulze et al. (2018) which included 53 H-poor and 16

H-rich SLSNe and hosts out to a redshift of 4, shows a growing population of SLSN hosts in the mass range $10^6 - 10^7 M_\odot$. It seems like there is a scarcity of hosts above $10^{10} M_\odot$ for both H-rich and H-poor SLSNe according to Schulze et al. (2018). The H-rich SLSNe, including SLSN-IIn, have very diverse hosts, but the lack of massive galaxies suggests some dependence on properties of the environment and a stifled production efficiency above 0.8 solar metallicity. In Angus et al. (2016), the hosts of regular CC SNe are compared to SLSNe and it is clear that the hosts are fainter and less massive for SLSNe than CC SNe, though this is most pronounced for the SLSNe-I (H-poor). However, H-rich SLSN hosts are also distinct from the CC SN host population, but the former span a larger range of magnitudes, which is consistent with the findings in Schulze et al. (2018).

3.2 The IIn Rate

To calculate the volumetric rate of type IIn, Equation (1) can be used, where volumetric means that the rate is per volume and the unit used here is Mpc^{-3}yr^{-1}. For any other type of CC SN, the ratio IIn/CC can be substituted with the ratio for another type, for e.g. IIb/CC.

$$rate_{IIn}(z) = \frac{IIn}{CC} \cdot k_{CC} \cdot SFR(z) \tag{1}$$

The IIn/CC ratio (or the ratio of any type of CC SN for that matter) is usually considered a constant and thus independent of redshift. The value of IIn/CC is quoted as 5% (Wojtak et al., 2019; Graur et al., 2017b) or 9% (Li et al., 2011a) (The 9% are calculated as the ratio to SNe II and not all CC SNe, and two of the SNe IIn have since been reclassified as SN impostors). This number is constrained by local (low-redshift) observations of CC SNe, which in practice means that the ratio of IIn to CC in the local Universe is simply extrapolated to apply to all redshifts. The rate also depends on the SFR, which is the star-formation rate in the Universe as a function of redshift, because of the short lifetimes of the CC progenitors. On astronomical timescales, the massive stars goes SN almost instantly after their creation. The factor k_{CC} describes how many CC SNe we expect and the value of k_{CC} depends on the initial mass function (IMF), since the IMF predicts the distribution of masses for a population of stars and so how many massive stars, CC SN candidates, there will be for a given population. The value adopted in our study is $k_{CC} = 0.011 M_\odot^{-1}$ from theoretical predictions of the Chabrier IMF (See Section 3.2.1).

3.2.1 Initial Mass Function

As mentioned in Section 3.2, the IMF characterizes the distribution of masses in a stellar population, but the shape of this distribution is an ongoing discussion. The first IMF was proposed by Salpeter (1955) and has the form of a simple power law:

$$\phi_S(M) = k_s \cdot M^{-\alpha_s}, \tag{2}$$

where k_s is the normalization constant (or the local stellar density constant) and $\alpha_s = 2.35$ is the slope. Since then, other forms have been proposed, most notably by Chabrier (2003), which modifies the form of the IMF for stars with masses less than $1M_\odot$:

$$\phi_C(M) = \begin{cases} k_C \cdot 0.158 \cdot \frac{1}{ln(10) \cdot M} \cdot e^{-\frac{(log_{10}(M) - log_{10}(M_C))^2}{2\sigma_C^2}}, & \text{if } M \leq 1M_\odot \\ k_C \cdot M^{-\alpha_C}, & \text{otherwise} \end{cases} \tag{3}$$

where k_C is the normalization constant, $M_C = 0.08$ is the mean mass, $\sigma_C = 0.69$ is the mass variance and $\alpha_C = 2.3$ is the slope when $M \geq 1M_\odot$. Also worth mentioning is the IMF proposed by Kroupa (2001):

$$\phi_K(M) = k_K \cdot \begin{cases} M^{-\alpha_{K1}}, & \text{if } M \leq 0.08M_\odot \\ M^{-\alpha_{K2}}, & \text{if } 0.08M_\odot \leq M \leq 0.5M_\odot \\ M^{-\alpha_{K3}}, & \text{if } M \geq 0.5M_\odot \end{cases} \tag{4}$$

where k_K is the normalization constant, and the slopes of the IMF for the different intervals are $M^{-\alpha_{K1}} = 0.3$, $M^{-\alpha_{K2}} = 1.3$ and $M^{-\alpha_{K3}} = 2.3$. And the IMF by Larson (1998) as well:

$$\phi_L(M) = k_L M^{-\alpha_L} \cdot \exp\left(-\frac{2.35M_{peak}}{M}\right), \tag{5}$$

where k_L is the normalization constant, α_L is the slope and M_{peak} is the peak mass. These two IMFs will not be further discussed in this thesis.

In Figure 8, the Salpeter and Chabrier IMFs are plotted for comparison. They are normalized such that $\int \phi(m)dm = 1$ and the lower and upper mass limits are usually assumed to be 0.08 and 100 $M_\odot$ (Hopkins, 2018), respectively, which is also the case in this work. From the figure, it is evident that the Salpeter IMF predicts more of the less massive stars than the Chabrier which is flatter for $M \leq 1M_\odot$. In the higher end of the mass range, Chabrier predicts more stars and so using Chabrier instead of Salpeter will result in more CC SNe. Conclusively, the choice of IMF

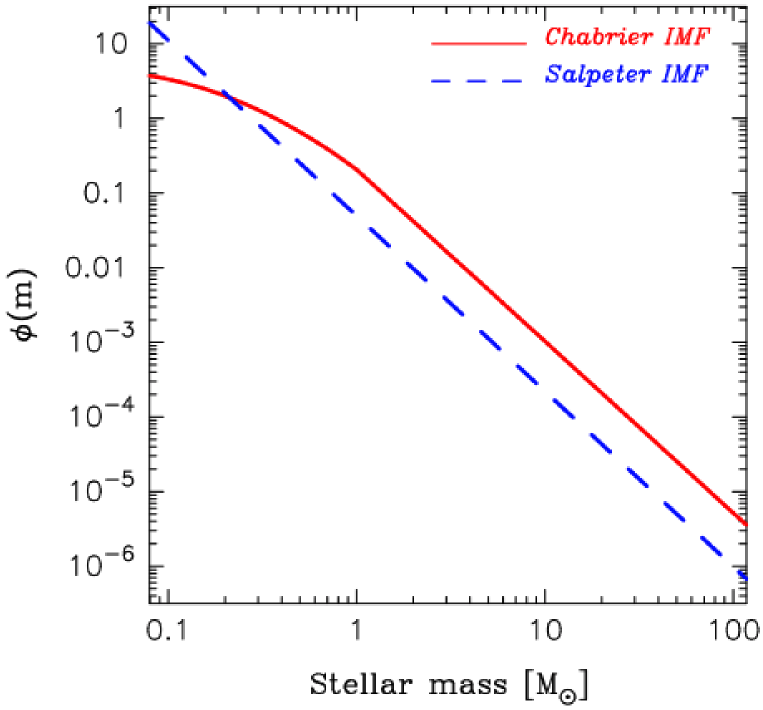

Figure 8: Comparison of Salpeter and Chabrier IMF from Shimizu & Inoue (2013).

matters because it will affect any result computed using the IMF as input. This also applies to k_{CC}, as the amount of SNe depends on the amount of massive stars. Yet it is possible to go from e.g. Chabrier to Salpeter by multiplying by 1.64 (this number will be different for scaling between other IMFs), because this is the ratio between the conversion factors κ_{FUV}. These conversion factors are used to convert the FUV-specific luminosity to SFR, and are different for every IMF. But as can be seen in Figure 9, the ratio depends slightly on age and metallicity (Madau & Dickinson, 2014).

k_{CC} can be determined from the IMF like so:

$$k_{CC} = \frac{\int_{m_{min}}^{m_{max}} \phi(m)dm}{\int_{m_l}^{m_u} m \cdot \phi(m)dm}, \tag{6}$$

where $\phi(m)$ is the IMF. The k_{CC} value can be determined for Chabrier IMF (with a normalization of $\phi(1) = 1.9 \cdot 10^{-2}$) as

$$\frac{\int_{8M_\odot}^{50M_\odot} 0.019 \cdot M^{-2.3} dM}{\int_{0.1M_\odot}^{1M_\odot} M \cdot \frac{0.158}{ln(10) \cdot M} \cdot e^{-\frac{(log_{10}(M) - log_{10}(0.08))^2}{2 \cdot 0.69^2}} dM + \int_{1M_\odot}^{125M_\odot} M \cdot 0.019 \cdot M^{-2.3} dM} = 0.011 M_\odot^{-1}. \tag{7}$$

which is as mentioned the value we choose to adopt for this thesis. These theoretical predictions are often used in SN rate calculations, but are backed by observational studies as well. Strolger

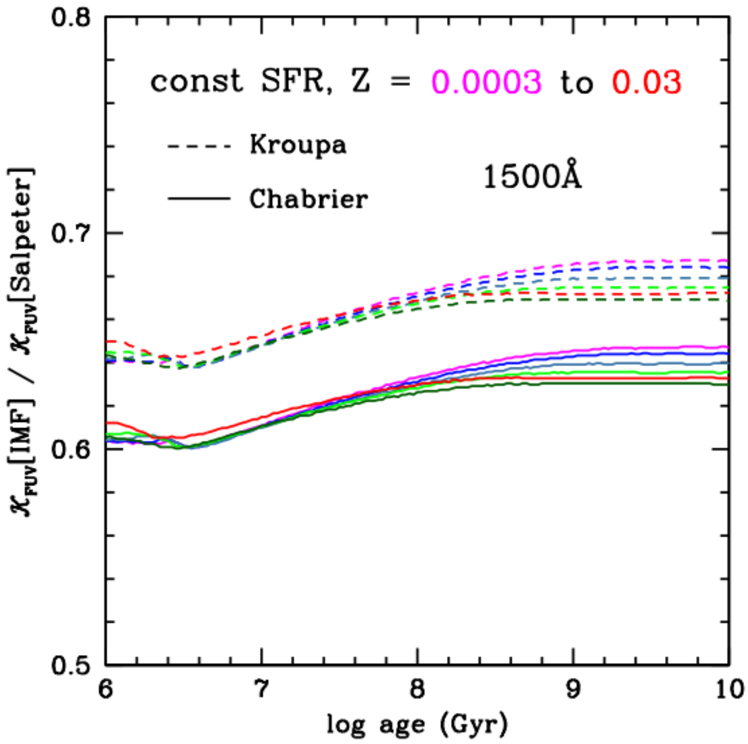

Figure 9: Ratio of κ_{FUV}s for Chabrier and Kroupa to Salpeter from Madau & Dickinson (2014) for different metallicities and constant SFR.

et al. (2015) find a value of $k_{CC} = 0.0091 \pm 0.0017 M_{\odot}^{-1}$ using the relation:

$$R_{CC}(z) = k_{CC} h^2 \psi_{UV}(z), \tag{8}$$

where h is the Hubble Parameter, and a weighted least squares fit of the star-formation history (SFH) model ψ_{UV} from Madau & Dickinson (2014) to the CC rate measures R_{CC} in Strolger et al. (2015). The SFH model derives from a fit to star-formation rate densities (SFRD) found by multiplying FUV luminosities with the conversion factor κ_{FUV} valid for the Salpeter IMF. As mentioned in Strolger et al. (2015), when using the Salpeter IMF one would except a k_{CC} value of $0.007^{+27\%}_{-31\%} M_{\odot}^{-1}$, which is within an acceptable range of uncertainty compared to $k_{CC} = 0.0091 \pm 0.0017 M_{\odot}^{-1}$.

The point to take away from this brief introduction to IMFs is the contribution to uncertainty in the calculation of the volumetric rate of CC SNe. The choice of IMF (and mass limits) will influence any results obtained and it is hence crucial to be transparent about IMF assumptions.

3.3 Cosmology & SNe IIn

Cosmology is seldom discussed in relation to SNe IIn. Most cosmologists are more interested in the prospects of SNe Ia, both lensed and unlensed, because of their unique standard candle properties mentioned briefly in Section 3, which provide some useful constraints for determining the expansion rate of the Universe. The intrinsic luminosity of lensed SNe Ia enables an independent check on lens models and so a more precise estimate of the Hubble constant (Pierel & Rodney, 2019). The Hubble constant and its relation to lensed SNe will be explained in Section 3.3.2. But as we will see in this section, SNe IIn can also be of use in a cosmological sense when gravitationally lensed.

This section will provide a short overview of the cosmological concepts needed to put the results and motivation of this thesis in a larger context and is not intended as an in-depth chapter on cosmology as this is outside of the scope of the thesis.

3.3.1 Gravitational Lensing

In some rare cases, SNe can be lensed by a foreground galaxy or cluster in our line of sight. Massive objects like galaxies bend spacetime around them as described by the theory of general relativity, and so can distort and bend light from e.g. SNe behind them. The light from the SN travels different paths through space around the lensing galaxy and produces several images of the same SN. An example is illustrated in Figure 10. The light is not only distorted by the lens, but it is also magnified allowing us to observe SNe that would normally be too faint to detect. This type of lensing is known as strong gravitational lensing. If the lens is not massive enough or sufficiently close to the source, the effect of lensing will not create multiple images, but can still distort the image by stretching or magnification on a smaller scale. This is known as weak gravitational lensing. Even objects such as stars can cause a lensing effect when passing in front of each other and this results in a slight magnification that is usually referred to as microlensing. Microlensing affects each of the images appearing from strong lensing separately and these effects introduce an uncertainty in any physical properties determined from the multiple images (Pierel & Rodney, 2019).

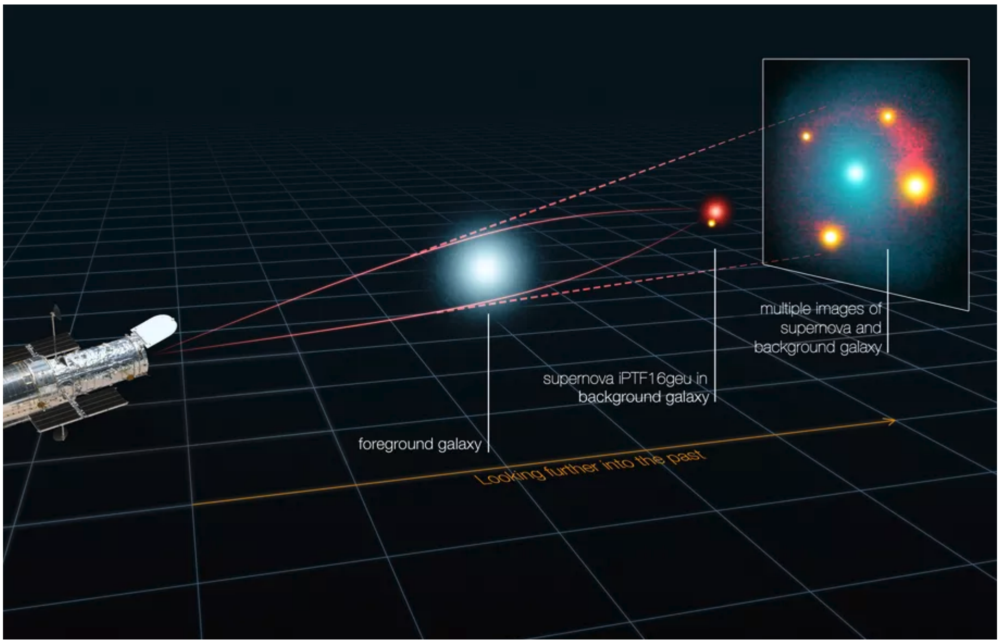

Figure 10: Schematic of strong lensing of the type Ia SN iPTF16GEU. Credit: ALMA (ESO/NRAO/NAOJ), L. Calcada (ESO), Y. Hezaveh et al., edited and modified by Joel Johansson.

3.3.2 Measuring the Hubble Constant

Strongly lensed SNe of any type can be used to measure the Hubble constant H_0 that describes the current expansion rate of the Universe. The value of H_0 has been measured using different and increasingly precise methods, and yet the values from these methods suggest a tension up to 5σ, a phenomenon known as the *Hubble tension*. This indicates that either our measurements are influenced by as yet unknown systematic errors and effects or a lack of complete understanding of the underlying cosmological model. Determining H_0 using type Ia SNe and Cepheids yields a value of 73.2 ± 1.3 km s^{-1} Mpc^{-1} (Riess et al., 2021) and from the cosmic microwave background (CMB) observations results in a value of 67.36 ± 0.54 km s^{-1} Mpc^{-1} (Planck Collaboration et al., 2018). Independent measurements of H_0 could help clarify the situation and give us better predictions for the future of our Universe. This is where lensing of SNe (and other astrophysical objects) comes in. As it was theoretically predicted by Refsdal (1964), it is possible to determine the Hubble constant from the time delays of the multiple images of a lensed SN. When the SN is lensed by a foreground galaxy, the light takes different paths through space as explained in Section 3.3 and this leads to the images appearing not only at different places but also at different times. In simple terms, the difference between the times when the light from the different images reaches the observer depends on the time-delay distance, $D_{\Delta t}$, which in turn depends on the Hubble constant as $D_{\Delta t} \propto H_0^{-1}$. This method is used on the multiply imaged CC SN Refsdal in Grillo et al. (2018), concluding that it is possible to measure H_0 with a comparable precision to the standard techniques using lenses. The value of H_0 based on early observations of SN Refsdal is found to be 64^{+9}_{-11} km s^{-1} Mpc^{-1} as calculated in Vega-Ferrero et al. (2018). This value is in agreement with the H_0 inferred from the CMB. Therefore, the effects of strong lensing make all subtypes of SNe, not only SNe Ia, useful for inferring cosmological parameters, with a larger sample of these objects ultimately resulting in very precise constraints on the Hubble constant. However, currently the different estimations of the Hubble constant are still pointing in different directions and so it seems the Hubble tension continues to be a subject of discussion for cosmological community.

3.3.3 Detection Methods

Lensed SNe are usually detected using two different methods, namely image multiplicity and magnification.

In image multiplicity, several of the multiple images of the supernova are resolved making this method more robust because the detection criteria are more stringent. When actually resolving more than one of the multiple images, one can be more confident in the classification of a lensed SN. But observing more of the images is difficult because it depends on the separation of the images relative to seeing, contrast in flux between the images and magnitudes of the faintest images of the SN (Wojtak et al., 2019). The strict criteria implies that we will only be able to detect a small part of the total number of lensed SNe in a given time interval.

The lensed SNe can also appear very bright, significantly brighter than what is expected at the redshift it is detected (redshift of the lens galaxy not the host galaxy). This is what is known as magnification. The detection criterion from Goldstein & Nugent (2017), as follows:

$$m_X(t_{peak}) < \langle M_X(t_{peak}) \rangle + \mu(z_{host}) + K_{XX}(z_{host}, t_{peak}) + \Delta m, \tag{9}$$

is dependent on the observed peak magnitude of the SN in a given band $m_X(t_{peak})$, the mean magnitude of a reference class of SNe $\langle M_X(t_{peak}) \rangle$, the distance modulus μ, the redshift of the host z_{host}, a K-correction $K_{XX}(z_{host}, t_{peak})$ and magnitude gap Δm between lensed and non-lensed SN. With this method, more supernovae can be detected and classified as lensed since the images do not need to be resolved. But when the criterion depends on the magnitude of a reference supernova class, for e.g. Ia's, certain classes like SLSNe could wrongly be identified as lensed.

So this method leaves us with less confidence in the lensed SN classification and depends on follow-up observations or light curve properties.

4 Data

The goal is to utilize the data from Lick Observatory Supernova Search (LOSS) (Graur et al., 2017b) and the UniverseMachine algorithm (Behroozi et al., 2019) to investigate the SNe IIn to CC ratio and the effect on the overall SNe IIn rate. In this section, the data is reviewed and discussed.

4.1 Lick Observatory Supernova Search

The Lick Observatory Supernova Search or LOSS SN sample, discovered using the 0.75 m Katzman Automatic Imaging Telescope (KAIT) at Lick Observatory, includes observations of SNe from 1998 to 2008 when the survey was in operation (Li, 2000; Graur et al., 2017a). In Graur et al. (2017b), a subsample of the LOSS SN sample is used to determine the fractions of different SN types in the sample. This subsample was constructed by Li et al. (2011a), with a complete description provided in Leaman et al. (2011).

LOSS discovered a total of 1036 SNe, with host galaxy information like Hubble type and redshift available for 929 of them. The subsample used in Graur et al. (2017b) was constructed using only SNe observed "in-season", which means that they exploded during the active monitoring of the host galaxies such that pre-peak observations are available, while and no SNe in small early-type galaxies (with major axis smaller than $1.0'$) were employed due to uncertain detection efficiency (Li et al., 2011a). By also using a cut-off distance of 80 Mpc for type Ia and 60 Mpc for CC SNe as well as not including SNe from later than 2006 (due to a reduced number of follow-up observations), the subsample contains 180 SNe in total, 74 type Ia, 99 CC and 7 SN imposters. Of the 99 CC SNe, 5 of them are type IIn, with their names and absolute magnitudes (Bilinski et al., 2015) listed in Table 1. SN2006am from LOSS exhibits properties of a IIn, but it may well be an imposter due to its faintness and blue continuum (Bilinski et al., 2015).

A completeness of 98$\%$ is achieved for Ia's out to 80 Mpc but only 80$\%$ for CC SNe out to 60 Mpc. To circumvent this, Li et al. (2011a) determined a so-called completeness correction for each SN in the sample. A sample is complete when no sources are "missed" within a certain volume or to a certain magnitude limit or during a time interval. In practice, a survey is never expected to be complete in itself, there are always some sources that cannot be observed for one reason or the other. Instead, one can estimate the degree of incompleteness and correct for this in different ways. In this case, Li et al. (2011a) are accounting for incompleteness in the time-domain using

SN	Peak Abs. Mag.	Host Galaxy
1999el	-18.4	NGC 6951
2003dv	-17.5	UGC 9638
2008fq	-18.1	NGC6907
2010jl	-20.6	UGC 5189A
2011A	-16.1	NGC 4902

Table 1: SNe IIn from the LOSS dataset and their peak magnitudes (Bilinski et al., 2015).

the quantity called control-time. Control-time is the amount of time a supernova is visible in a given galaxy and this depends on the light curves and peak magnitudes of the SNe as well as the limiting magnitude of the instrument and the distance to the galaxy (Barbon, 1968). If the cadence is smaller than or equal to the control-time, no SNe of that type would be missed, but this is not possible as mentioned earlier, for eg. due to bad weather or the position of the SN in the sky. This is what is taken into account with the completeness corrections. A detailed overview of the mathematical formalism, numerical processes and light curve fits underlying these corrections can be found in Leaman et al. (2011), Li et al. (2011b) and Li et al. (2011a), respectively.

Now the incompleteness of the SNe was dealt with, but the host galaxy sample is a different story. The galaxies do not accurately represent the luminosity distribution within 80 or 60 Mpc. The sample is deficient in the lower luminosity end of the scale because LOSS is a targeted survey. In a targeted survey, specific galaxies are monitored over time in the hopes of detecting SNe and this is both more difficult and less rewarding to do for small faint galaxies. The incompleteness in the galaxy sample could possibly affect the SN rates and this will be further discussed in Section 4.1.1.

4.1.1 Relative Rates

The goal of the study by Graur et al. (2017b) is to compare the relative rates of the different SN types found in the LOSS subsample for low- and high-mass galaxies, although 21 of the host galaxies do not have LOSS masses, which renders the comparison difficult. In this case, it is not possible to simply remove the 21 SNe as this would leave the sample incomplete and the relative rates would no longer reflect the true rates. Instead, Graur et al. (2017b) estimate the masses using the rest of the galaxies in the sample. As can be seen in Figure 11, there is a correlation between stellar mass and luminosity in B- and K-bands for the galaxies and either K- or B-band luminosity is available for all galaxies in the sample. To estimate the masses of the 21 galaxies, the median stellar mass value in a bin of 0.2 dex corresponding to the galaxies' luminosity in either B- or K-band is chosen, and the uncertainty is given by the 16th and 84th percentile. As noted by Graur et al. (2017b), the masses of the 21 galaxies are spread out over the mass range, which means that the estimations are unlikely to induce a systematic bias in their analysis.

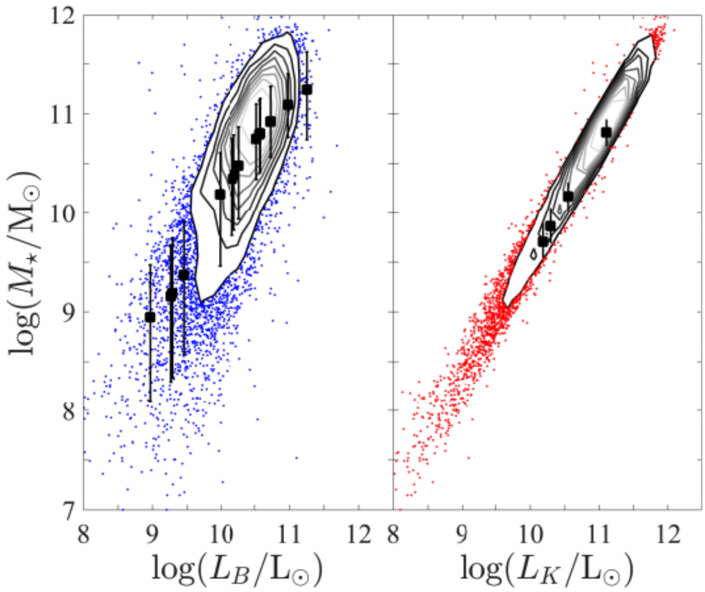

Figure 11: Stellar mass vs B-band (left) or K-band (right) luminosity. The 21 estimated galaxy masses are shown as black squares. Figure from Graur et al. (2017b).

The data set is split into a low-mass part and a high-mass part according to different mass cuts: $3\times10^9 M_\odot$, $10^{10} M_\odot$ and $3\times10^{10} M_\odot$ and the fractions of SNe types are calculated for host galaxies on either side of the cut. It is subsequently possible to compare the SN subtype fractions for low- and high-mass galaxies. Graur et al. (2017b) run 1000 Monte Carlo simulations to estimate the uncertainty on the fraction of each SN before calculating the resultant fractions with uncertainties. The classification of some SNe can be uncertain and so they are assigned a classification weight for each possible classification depending on which one is more likely and this is taken into account with the Monte Carlo simulations as well as the effect of the estimated masses as their values are varied to test for the effect of filling. The relative CC SN rates are visually presented in Figure 12. More in-depth information, including Ia's, can be found in Table 1, A1 and A2 in Graur et al. (2017b). These are the fractions and uncertainties that constitute the basis of the analysis in this thesis.

In Graur et al. (2017b), it is argued that the galaxy sample incompleteness does not introduce any bias in the results as low-luminosity galaxies do not produce many SNe due to the low SFR. Moreover, the LOSS sample does contain around 29% of galaxies with stellar masses below $10^{10} M_{\odot}$ that should represent low-luminosity galaxies well as there is no reason to suspect them being odd cases. However, this argument is not very strong. When the goal is to compare fractions of SN types between low- and high-mass galaxies within a volume and the sample is incomplete in the low-luminosity or low-mass end of the range, this could have a significant effect on the results in both Graur et al. (2017b) and this thesis, which will be discussed in Section 6.

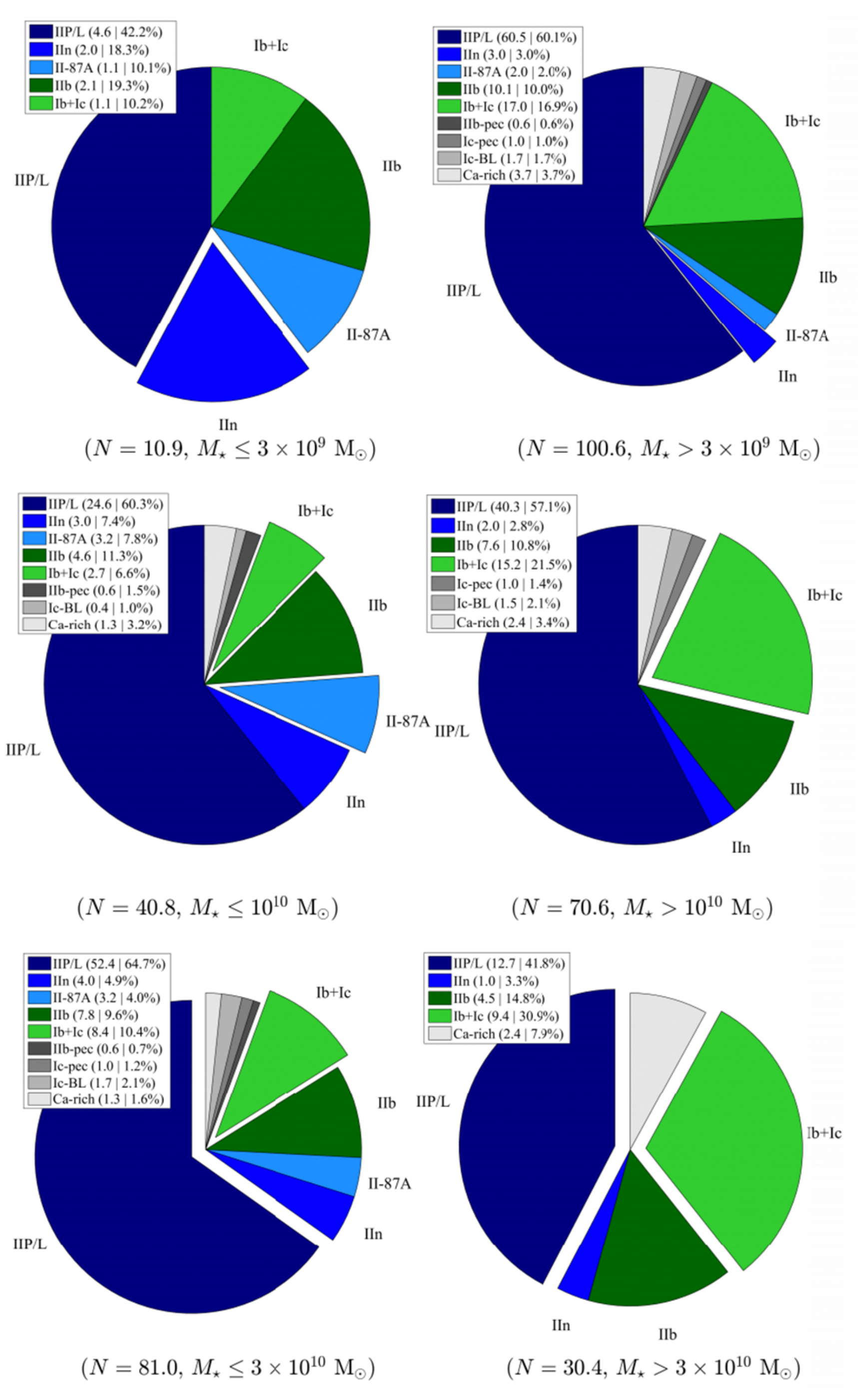

Figure 12: Relative CC SN rates for all three mass cuts. N is the number of SNe and M_* denotes the stellar mass of the host galaxy. Figure adapted from Graur et al. (2017b).

4.2 UniverseMachine

As mentioned in Section 3.2, the rate of type IIn SNe depends on the IIn/CC value as well as the SFR. The IIn to CC ratio comes from results by Graur et al. (2017b) as explained in Section 4.1.1, so now the only part missing is the SFR. To calculate this, I use the results from the UniverseMachine algorithm by Behroozi et al. (2019). A schematic of the process behind UniverseMachine is illustrated in Figure 15. The code starts from a parametrization of galaxy SFRs as a function of dark matter halo potential well depth, which in turn depends on the maximum circular velocity of the halo v_{max}. Galaxies form at the centers of the gravitationally bound dark matter structures known as halos and according to several studies (for e.g., see review by Wechsler & Tinker, 2018), the growth and size of galaxies can be linked to the growth and size of the halos. The relation between SFR and v_{max} is then applied to a dark matter simulation, thereby creating a "mock universe" as explained in Behroozi et al. (2019), which is afterwards compared to real observations of our Universe and a Bayesian likelihood is calculated. A Markov Chain Monte Carlo algorithm is subsequently used to make a new guess of the SFR-v_{max} relation, repeating the whole process until we get a full picture of the range of SFR-v_{max} parametrizations agreeing with observations. Behroozi et al. (2019) assume a Chabrier IMF and adopt a flat ΛCDM cosmology with parameters consistent with Planck (Ade et al., 2016).

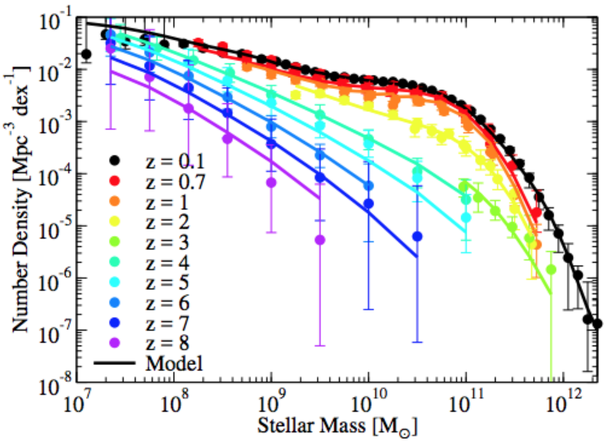

Figure 13: Stellar mass function observations compared to the results of UniverseMachine indicated by the solid line (Model). Figure from Behroozi et al. (2019).

The results of the simulation are best-fitting models of stellar mass functions (SMFs), cosmic star formation rates (CSFRs), specific star formation rates (sSFRs), UV luminosity functions

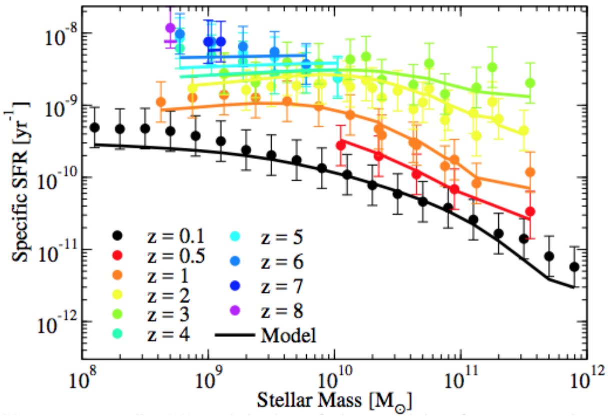

Figure 14: Specific star-formation rate (sSFR) observations compared to results of UniverseMachine (model). Figure from Behroozi et al. (2019).

(UVLFs) and so on. One can determine the SFR as (see Figures 13 for SMFs and 14 for sSFRs):

$$SFR = \int_{M_{min}}^{M_{max}} SMF \cdot M \cdot sSFR \; dM. \tag{10}$$

When calculating the SFR this way, one can split it into different mass bins in order to see the contribution to the total SFR from galaxies of different masses and how this changes with redshift.

The UniverseMachine resulting models have mass ranges of $10^7 M_\odot$ to $10^{13} M_\odot$ and redshift values from around zero to around 17. These values are actually given as the scale factor a in the data and not redshift, but are converted to redshift using equation (11):

$$z = \frac{1}{a} - 1. \tag{11}$$

The mass range of the UniverseMachine data set will be used as limits for the models proposed in Section 5.

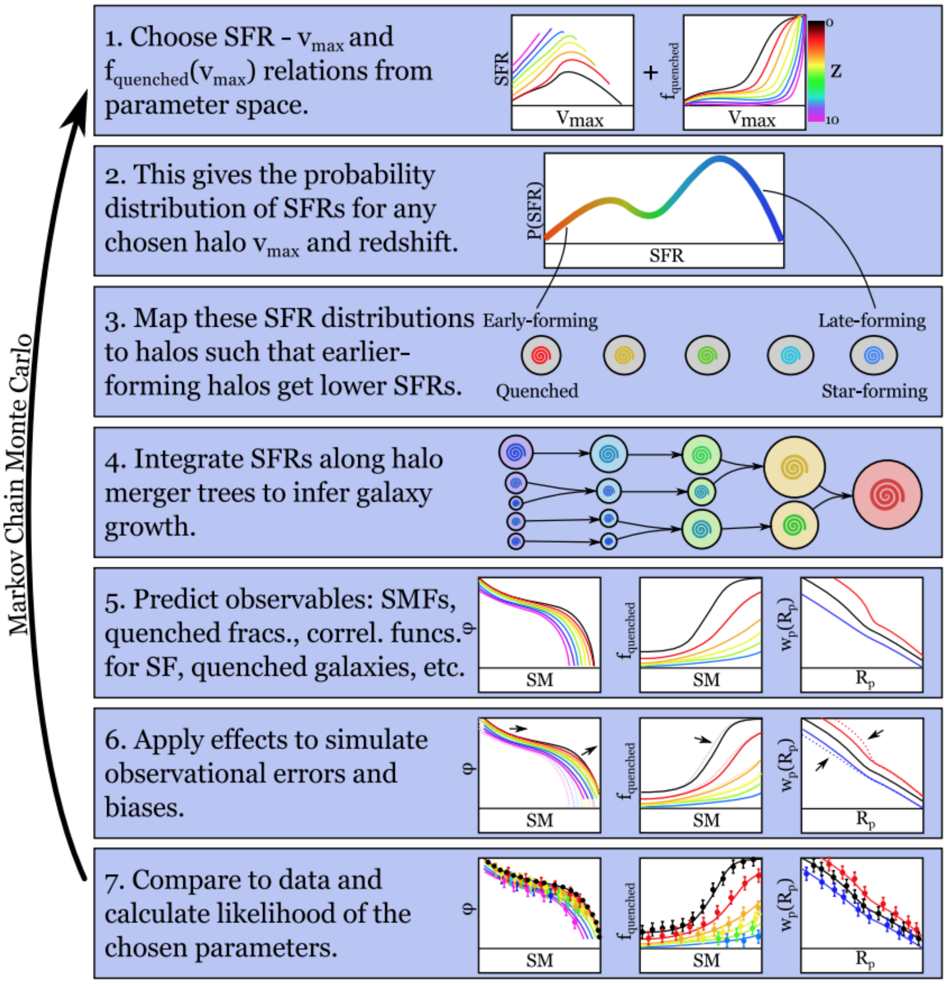

Figure 15: A schematic of the process behind the UniverseMachine algorithm. Figure from Behroozi et al. (2019).

5 Method and Results

To begin the analysis, the host galaxy mass values corresponding to every SNe IIn to CC ratio from Graur et al. (2017b) is chosen arbitrarily within the respective mass cut intervals. This is plotted in Figure 16. The x-axis error bars symbolize the mass cuts.

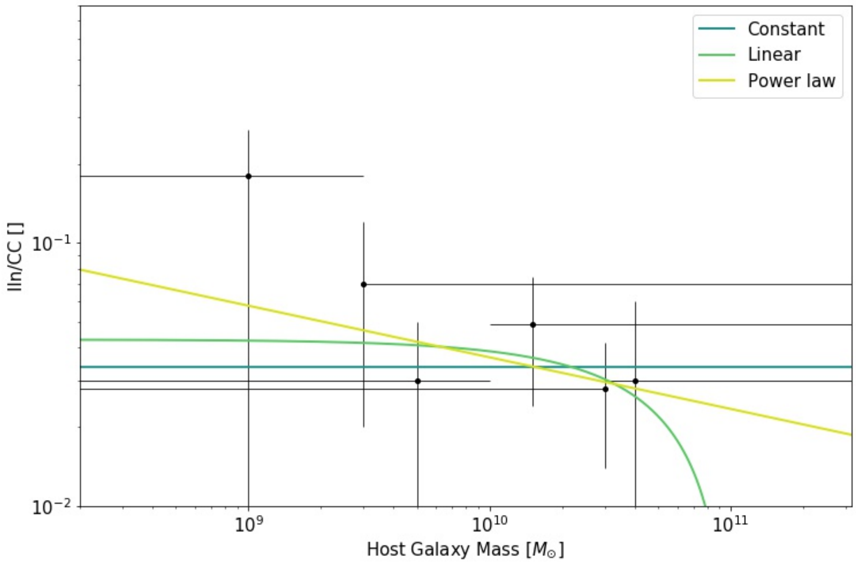

Figure 16: IIn/CC fractions from Graur et al. (2017b) plotted on either side of the respective mass cut values as well as three fitted models.

Figure 16 also shows three fitted models; one is constant, one is linear and one is a power law. Since the fits are only used as an indicator for the best choice of model, we choose not to use the asymmetric uncertainties as this plot only serves to illustrate why a specific model is chosen over another. Instead the largest part of the uncertainty is used as symmetric uncertainty in the fit. Since the linear model goes to zero at around $10^{11} M_\odot$, this model is not ideal as it predicts no type IIn SNe in galaxies with a mass larger than $10^{11} M_\odot$, which is not meaningful. As such, we discard this model. The power law, however, could be a good choice as it does not predict any unphysical values. Moreover, it is a simple model, which is a desired trait for problems involving a modest volume of data. The chosen model shape to use in further analysis in later sections is the power law as seen in Equation (12):

$$IIn/CC(M) = A \cdot M^k. \tag{12}$$

It is also worth noticing that the constant model does seem to agree with the data at first glance. In our analysis, all results will be compared to the constant model, which is the one currently used in the astrophysics community. It is evident from the fits that both the constant and power law models are valid for describing the relationship between the SNe IIn to CC ratio and the host galaxy stellar mass, and so we cannot rule out a bias towards lower mass hosts for SNe IIn.

5.1 Model Constraints

Given the nature of the data, performing a formal fit is rather complicated, so instead we ensure that the models agree with the data using 7 different constraints. Given different values of A and k, a model is only "good" if it satisfies these constraints. The first constraint (Equation (13)) comes from the total number of SNe IIn. In the LOSS subsample, there are 111.4 CC SNe after completeness correction and $5 \pm \sqrt{5}$ of these are SNe IIn (Graur et al., 2017b). As seen in Equation (13), this gives a IIn to CC ratio (R(IIn/CC)) of 0.045 ± 0.020 using error propagation:

$$R(IIn/CC) = \frac{5 \pm \sqrt{5}}{111.4} = 0.045 \pm 0.020. \tag{13}$$

As described in Section 4.2, the mass range of the Universe Machine will be used as range for these models. So, within the interval of $10^7 M_\odot$ to $10^{13} M_\odot$, the models must predict the number of IIn and CC SNe given by the data, which is the explanation behind Equation (14). The integral in the denominator is the normalization.

$$\frac{\int_{10^7 M_\odot}^{10^{13} M_\odot} A \cdot M^k dM}{\int_{10^7 M_\odot}^{10^{13} M_\odot} dM} = 0.045 \pm 0.020 \tag{14}$$

The other 6 constraints derive from the mass cuts found in Table 1, Table A1 and Table A2 in Graur et al. (2017b). Within the limits of the mass range and the value of the mass cut, the models must predict the right SNe IIn to CC ratio given in the aforementioned tables in Graur et al. (2017b) within the uncertainty. Hence, there are two constraints per mass cut value. The 6 constraints are as follows:

$$\frac{\int_{10^7}^{3 \cdot 10^9} A \cdot M^k dM}{\int_{10^7}^{3 \cdot 10^9} dM} = 0.18^{+0.09}_{-0.18} \tag{15}$$

$$\frac{\int_{3 \cdot 10^9}^{10^{13}} A \cdot M^k dM}{\int_{3 \cdot 10^9}^{10^{13}} dM} = 0.03 \pm 0.02 \tag{16}$$

$$\frac{\int_{10^7}^{10^{10}} A \cdot M^k dM}{\int_{10^7}^{10^{10}} dM} = 0.07 \pm 0.05 \tag{17}$$

$$\frac{\int_{10^{10}}^{10^{13}} A \cdot M^k dM}{\int_{10^{10}}^{10^{13}} dM} = 0.028 \pm 0.014 \tag{18}$$

$$\frac{\int_{10^7}^{3\cdot 10^{10}} A \cdot M^k dM}{\int_{10^7}^{3\cdot 10^{10}} dM} = 0.049 \pm 0.025 \tag{19}$$

$$\frac{\int_{3\cdot 10^{10}}^{10^{13}} A \cdot M^k dM}{\int_{3\cdot 10^{10}}^{10^{13}} dM} = 0.03 \pm 0.03. \tag{20}$$

If a model fulfills the above constraints, it will be considered as a good model to describe the data and will be used in further analysis. However, these models are not weighted with the mass function, which means that the choice of upper mass limit dominates the results. In fact, the constraints should have been in something like the following form:

$$\frac{\int_{M_{min}}^{M_{max}} A \cdot M^k \cdot SMF(z, M) dM}{\int_{M_{min}}^{M_{max}} SMF(M, z) dM}. \tag{21}$$

In this way, the distribution of galaxy masses is taken into account. Failure to do so will cause the power law solutions to favour one extreme end of the range, and assign equal probability to all solutions, which is not necessarily the case. However, this effect has not been taken into account in this thesis due to shortage on time, as this problem was not discovered until shortly before deadline.

5.2 Power Law Models

In order to choose values of A and k, we construct a grid. We choose values between -0.25 and 0.0001 for k with steps of 0.01, while for A, we choose between 0 and 25 with steps of 0.02. These values are mostly arbitrary but motivated by the shape of the function, as can be seen from Figure 16, which requires positive values of A and negative values of k. All the combinations of A and k values are tested to see if they fulfill the conditions from Section 5.1. With this specific grid, we find 207 good models to use in further analysis. The grid can be seen in Figure 18.

The 207 solutions are plotted in Figure 17. In this figure, a constant model with uncertainties is also plotted. We investigate what values of R(IIn/CC) would be good choices for a constant

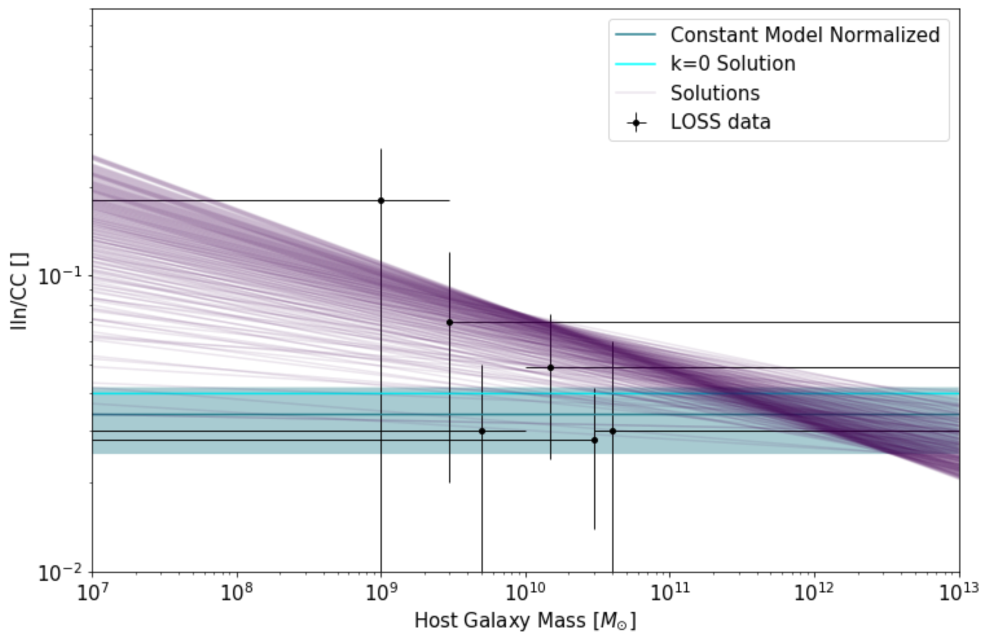

Figure 17: The 207 power law models plotted over the results from Graur et al. (2017b) and the constant model with uncertainties. The $k = 0$ power law solution is highlighted.

model, meaning that these values would agree with the data and compare to other estimates of the local ratio. Following the same logic as in the former section,

$$\frac{\int_{10^7 M_\odot}^{10^{13} M_\odot} x \; dM}{\int_{10^7 M_\odot}^{10^{13} M_\odot} dM} = 0.045 \pm 0.020. \tag{22}$$

But since the model is only a constant, equation (22) simplifies to:

$$x = 0.045 \pm 0.020. \tag{23}$$

This means that in order for the constant model to fulfill all seven constraints, we must find the interval of values that all constraints agree on. To do this, we examine the conditions, their values and uncertainties and find that the range of values acceptable for the constant model is 0.025 to 0.042. To express this as a mean and uncertainty:

$$x = 0.034 \pm 0.009. \tag{24}$$

This value is plotted in Figure 17 as the constant model. It is interesting to notice that in the 207 solutions, there is one $k = 0$ solution or constant solution. As can also be seen in Figure 17, this specific solution is consistent with the constant model predictions.

As mentioned in the previous section, the solutions in this figure cannot be seen as a probability density because of the way they are chosen in the A and k plane from the conditions. This means that the more solutions we have in a certain area does not mean that these solutions are more probable and better choices for describing the data. The distribution of solutions is visualized in Figure 19 for each constraint, and here we do in fact see exactly how the solutions favour one end of the range for most of the seven constraints.

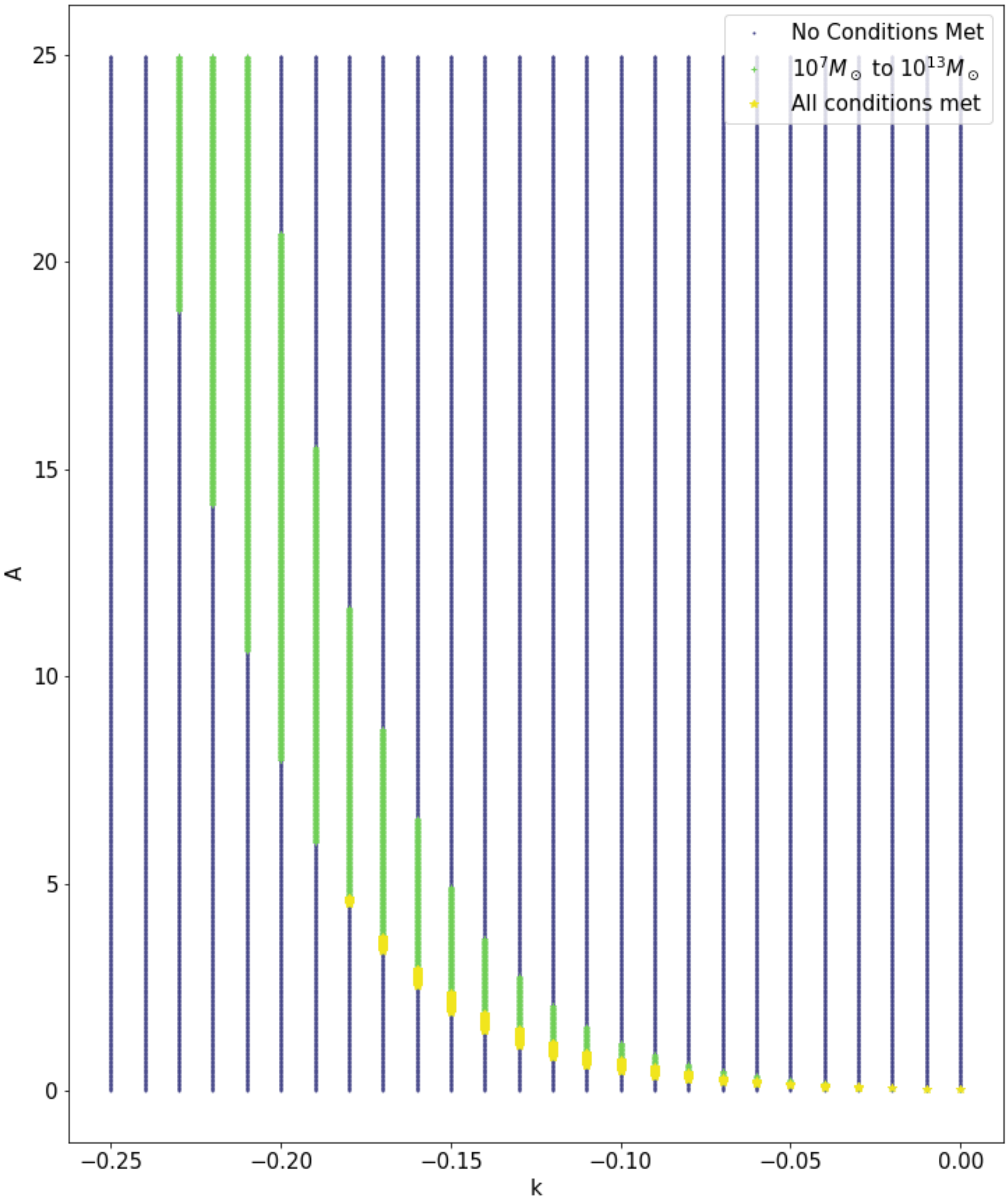

Figure 18: Grid of A and k values. The pairs in purple do not fulfill any of the constraints, while the ones in green satisfy at least one constraint (Equation (14)) and the yellow ones fulfill all constraints.

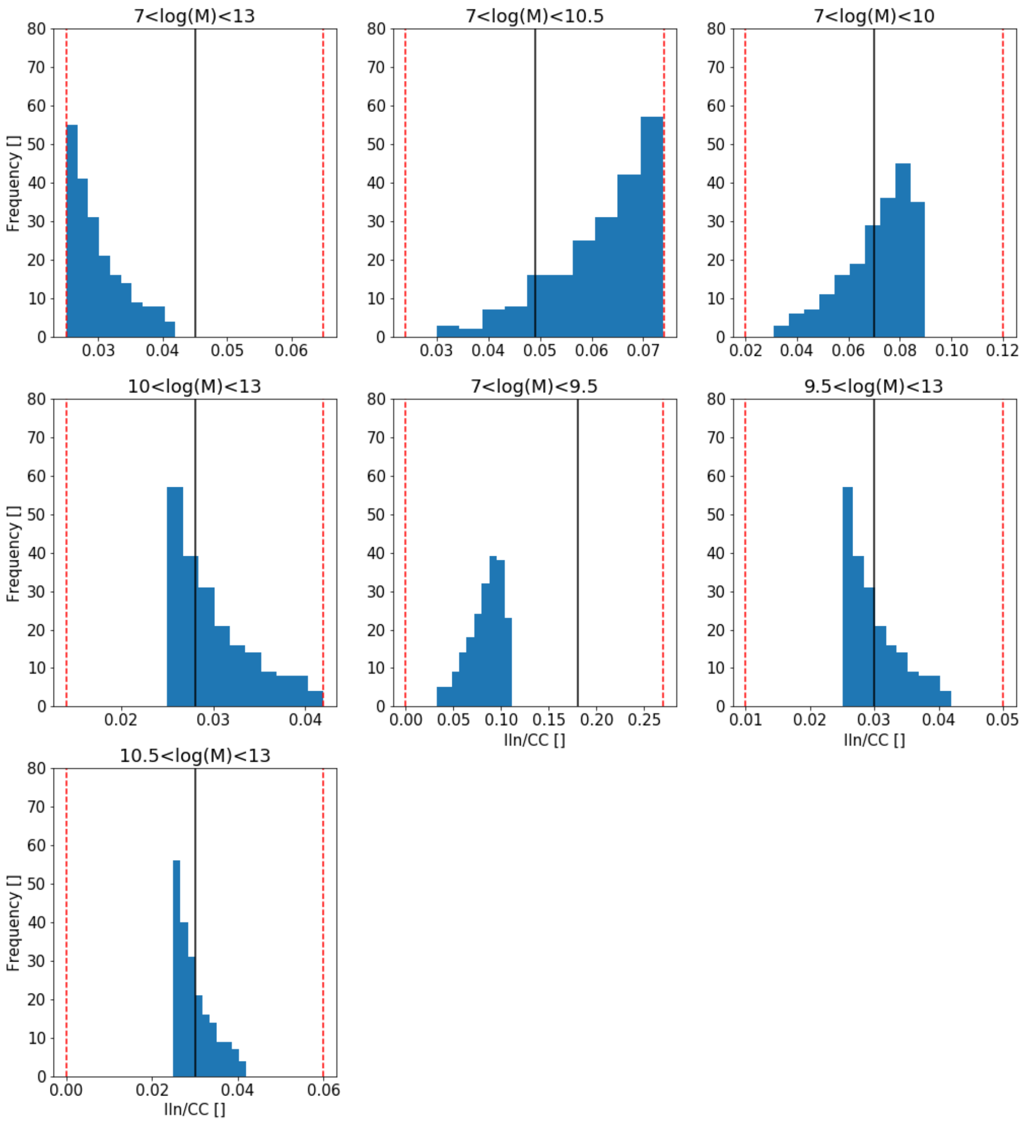

Figure 19: Distribution of solutions for each constraint. The black solid line marks the mean value of the constraint, and the red dashed lines indicate the uncertainty.

5.3 Star Formation Rate

Now that the power law models of IIn/CC are chosen, the next step is to look at the SFR and the UniverseMachine data. The Universe Machine data release 1 can be found at `peterbehroozi.com/data.html`. As described in Section 4.2, we primarily use the SMFs, with an example illustrated in the top left panel in Figure 20. The SMFs are multiplied by the mass and sSFR as shown in Equation 8 and depicted in the top right panel of Figure 20.

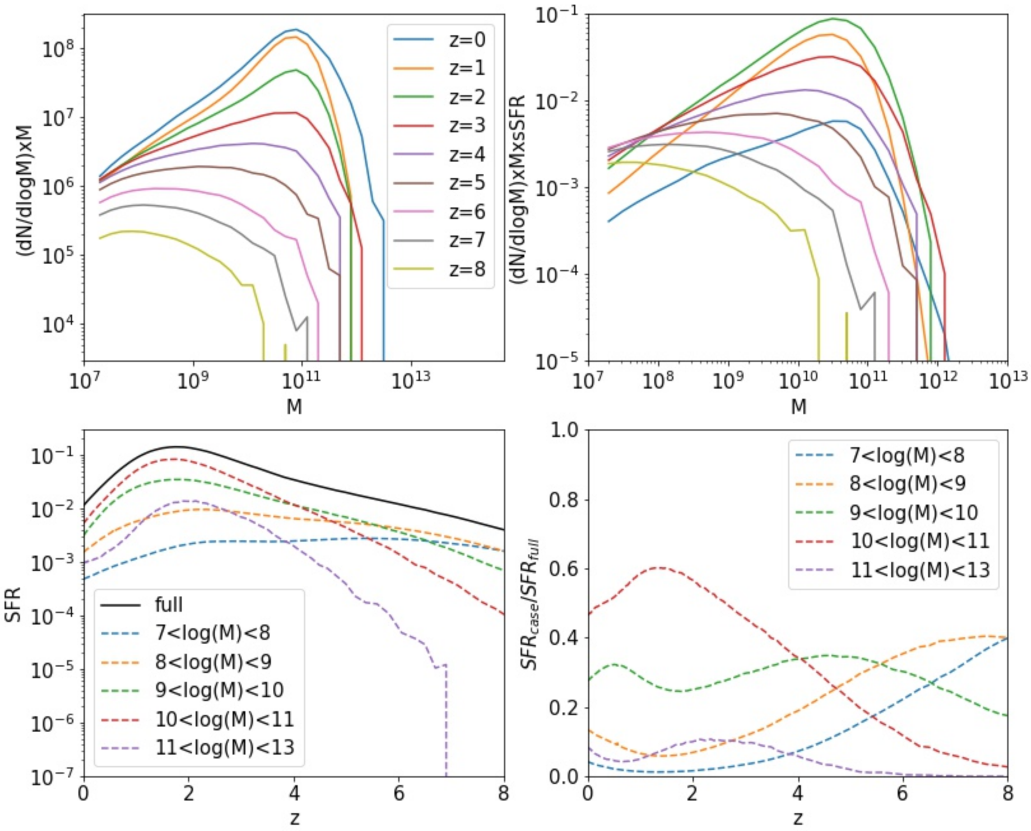

Figure 20: (*Top left*) Examples of the SMFs from the Universe Machine data for redshifts 0 to 8. (*Top right*) The example SMFs multiplied by mass and sSFR for the same redshift values. (*Bottom left*) The resulting SFR for the chosen mass bins and the total SFR. (*Bottom right*) Every SFR mass bin divided by the total SFR.

We opt to define five different mass bins; $7 < \log(M) < 8$, $8 < \log(M) < 9$, $9 < \log(M) < 10$, $10 < \log(M) < 11$ and $11 < \log(M) < 13$, and compute the contribution to the total SFR for each mass bin. The result, as well as the total SFR, can be seen in the bottom left panel in

Figure 20. The reason that the last mass bin does not have the same width as the other four is that the contribution from the galaxies in the range $12 < \log(M) < 13$ is close to none. As a check, the SFR for each mass bin is divided by the total SFR and plotted in the bottom right panel of Figure 20. Here, it is shown that the smaller galaxies have an increasingly larger contribution with higher redshift as expected, as there should be more of the less massive galaxies in the earlier Universe. In other words, the results make physical sense, providing a consistency check for the calculations carried out above.

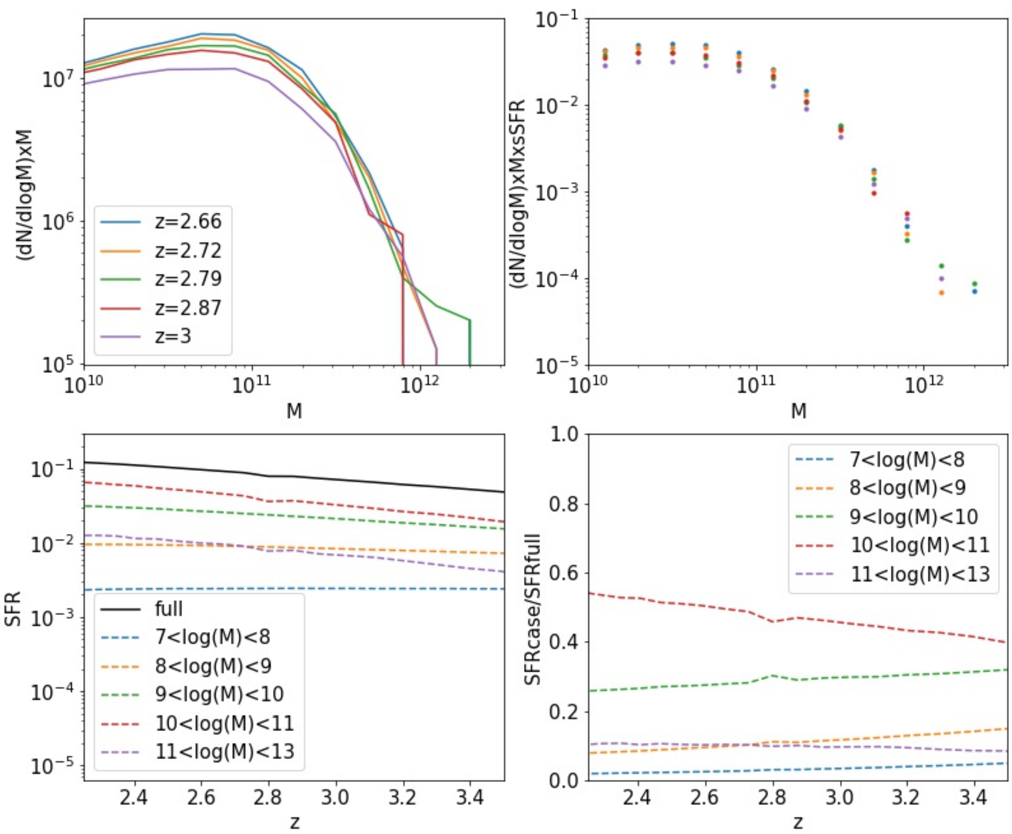

Figure 21: (*Top left*) SMFs for redshift values from 2.66 to 3, zoomed in to a mass range of $10^{10} M_{\odot}$ to $10^{12.5} M_{\odot}$. (*Top right*) SMFs multiplied by mass and sSFR for the same redshift values and mass range. (*Bottom left*) The SFRs zoomed in to a redshift range of 2.25 to 3.5 where the glitch is visible. (*Bottom right*) SFR bins divided by the total SFR and zoomed in on the glitch.

During the initial analysis and calculations, a small and unphysical "bump" kept showing up in the plots as can be seen in the bottom panels in Figure 21. To investigate the source of this issue, the SMFs in the affected redshift range were plotted as shown in the top panels in Figure 21. The plots are also limited to the affected mass range, as the bump seems to be only visible for the $9 < \log(m) < 10$ and $10 < \log(M) < 11$ mass bins. As can be seen in the top left and top right panels of Figure 21, the SMF for a redshift of 2.87 unexpectedly crosses the other SMFs, causing the bump seen in the SFRs. As this only happens at this particular redshift in a particular mass range, one must assume that it is a glitch in the simulation and not predicting anything physical. That is why the glitch has been removed for the resulting SFRs shown in Figure 20.

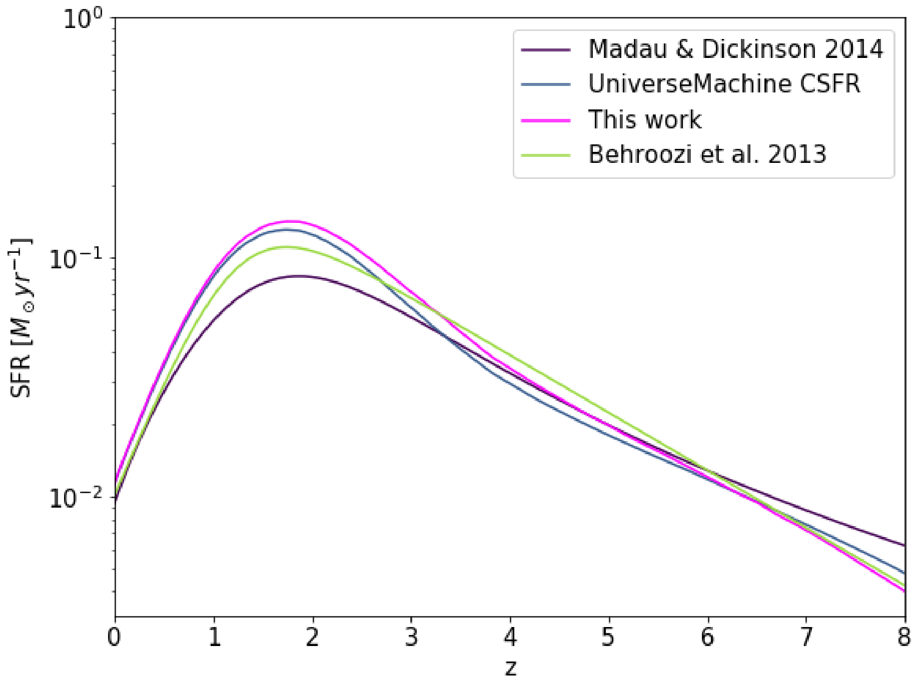

Figure 22: Comparison of the total SFR in this work, the CSFR from the Universe Machine data release, the CSFR parametrization from Behroozi et al. (2013) and the CSFH paramterization from Madau & Dickinson (2014).

In Figure 22, the total cosmic SFR (CSFR) calculated in this work is compared to suggested parametrizations of the CSFR and also the CSFR data from the Universe Machine simulation. The parametrization from Madau & Dickinson (2014) can be found in Equation (25) below:

$$\psi(z) = 0.015\frac{(1+z)^{2.7}}{1+((1+z)/2.9)^{5.6}} M_\odot \mathrm{yr}^{-1}\mathrm{Mpc}^{-3}. \tag{25}$$

And the parametrization from Behroozi et al. (2013) is provided in Equation (26):

$$CSFR(z) = \frac{C}{10^{A(z-z_0)} + 10^{B(z-z_0)}}, \tag{26}$$

where A, B, C and z_0 are constants given as -0.997, 0.241, 0.180 and 1.243, respectively (see Equation F1 and Table 6 in Behroozi et al. (2013)). The first is based on a Salpeter IMF and the latter on Chabrier, all values are converted to a Chabrier IMF in Figure 22. The comparison is done as an additional check of the SFR calculation in this work, but even though the different CSFRs are very similar, none of them are identical. This could be explained by the data that the parametrizations and algorithms are based on. However, for the purposes of this thesis and the uncertainties involved, the CSFRs are consistent and the calculated total SFR in this work can be used for determining the SNe IIn rate in the next section.

5.4 IIn Rate

Next, the IIn volumetric rate can be determined using Equation 1, combining the power law models and the results of the SFR calculations.

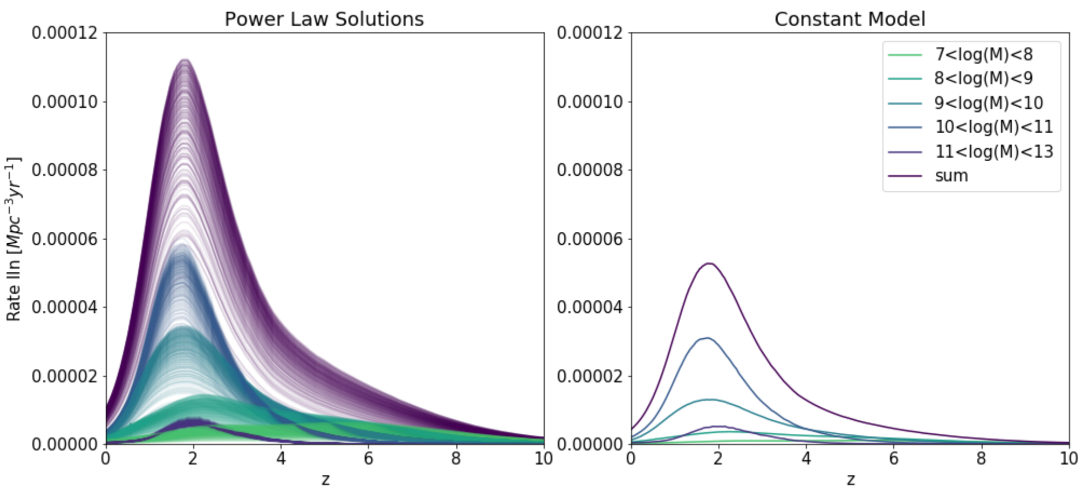

Figure 23: The IIn volumetric rates for every mass bin, as well as the total rate, from the 207 power law models (*left panel*) and from the constant model (*right panel*).

We calculate R(IIn/CC) for each mass bin using the center host galaxy mass bin value and the values of A and k for each power law model. The R(IIn/CC) values are then used to compute the SNe IIn rate for every mass bin and finally combined to find the total volumetric rate. The results of these calculations are displayed in Figure 23.

6 Discussion

In the literature, the local SNe IIn to CC ratio have historically been quoted from different studies with slightly different values (two of them mentioned in Section 3.2). The value of the ratio depends strongly on the quality of the data used and the accuracy of the SN classifications. For this work, the local ratio has been estimated to be 0.034 ± 0.009 (Equation 24), from the constraints and under the assumption that the ratio must be constant. This value is different from and inconsistent with the 0.05 used in Wojtak et al. (2019), determined from only the total number of SNe IIn and CC.

In Section 5.2, the 207 power law models are found using a grid of A and k values with a resolution of 0.02 for A, and 0.01 for k within an interval of 0 to 15 and -0.25 to 0, respectively. Increasing the resolution of the grid does not have a significant effect on where the "good" models are found, but only enhances the shape of the models fulfilling all seven conditions as in Figure 18. Expanding the grid for negative A yields no solutions, while for positive k we see a few for a grid size of 0.009 for k and 0.01 for A out to $k = 0.05$, but no significant change. No further solutions are found for k smaller than -0.25 and expanding A out to 17.5 yields a few additional solutions, but again no significant change.

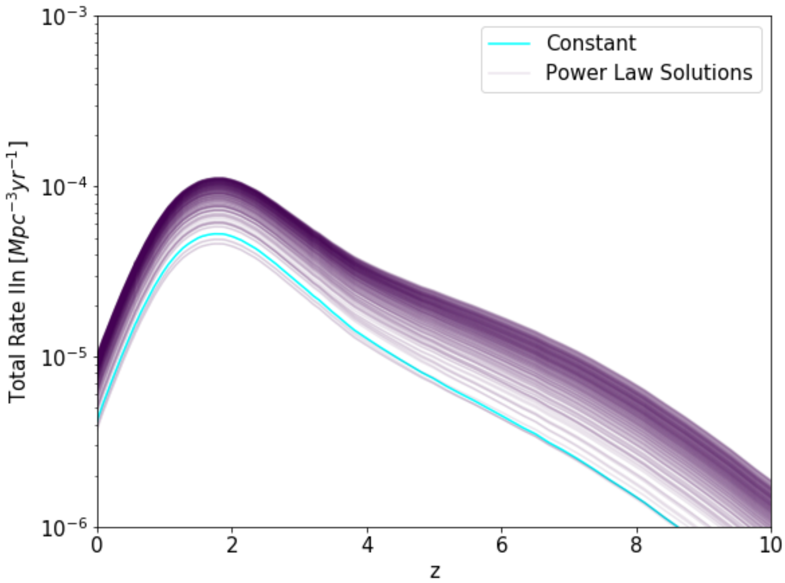

Figure 24: The total rate calculated from the power law models compared to the rate from the constant model.

Most of the power law solutions are predicting a higher rate than that predicted by the constant model. This can be seen if we compare the rate for the different solutions in Figure 24. The overall higher rate results from the propagated uncertainties from the constraints and model selection. The density of models is higher at the more extreme end of the range. However, as previously stated, this does not imply that the models in this range are more likely. The interpretation is that there is a non-zero probability for the total SNe IIn rate to fall within the range of models shown in Figure 24.

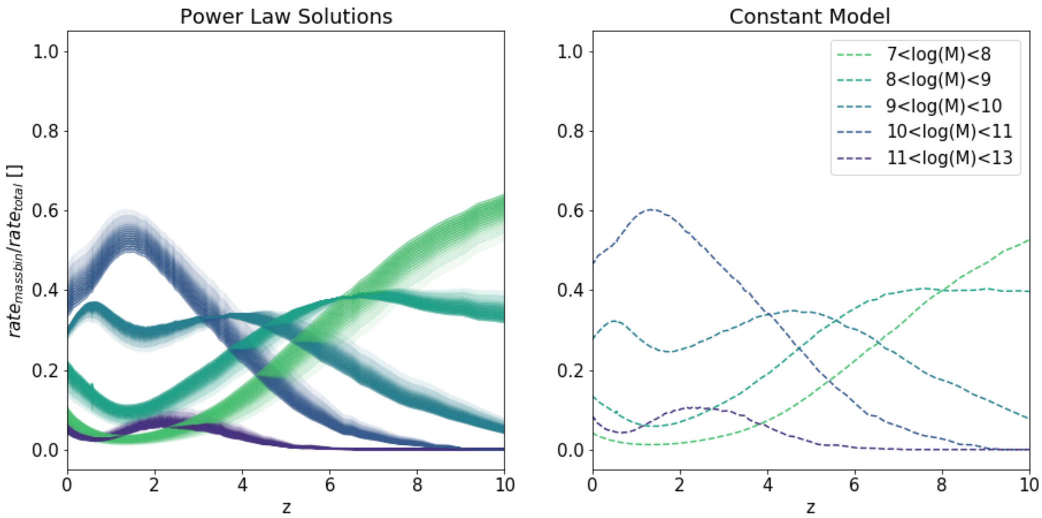

Figure 25: (*Left panel*) The ratio of the rates from each mass bin to the total rates calculated from the power law models. (*Right panel*) Ratio of the rate from each mass bin to the total rate for the constant model.

From Figure 25, it is clear that the less massive galaxies contribute more to the total IIn rate for the more extreme power law models compared to the constant model. We see an overall drop in the rate for the mass bins $10 < \log(M) < 11$ and $11 < \log(M) < 13$, while there is a bigger contribution from the $8 < \log(M) < 9$ and $9 < \log(M) < 10$ bins for smaller redshifts and a drop for higher redshifts, at $z = 7$ and $z = 4$, respectively. For the $7 < \log(M) < 8$ mass bin, we see a bigger contribution to the total rate for the power law models over all redshifts when comparing to the constant model. In Figure 26, the ratio of power law models to constant model for each mass bin is shown. The power law models predict higher rates overall but especially for the $7 < \log(M) < 8$ mass bin and also for higher redshifts. In general, the effect of a higher contribution from the lower mass galaxies is the most visible after redshift 4, which can also be seen in Figure 24, where the more extreme power law models predict a bump in this area compared to the constant model.

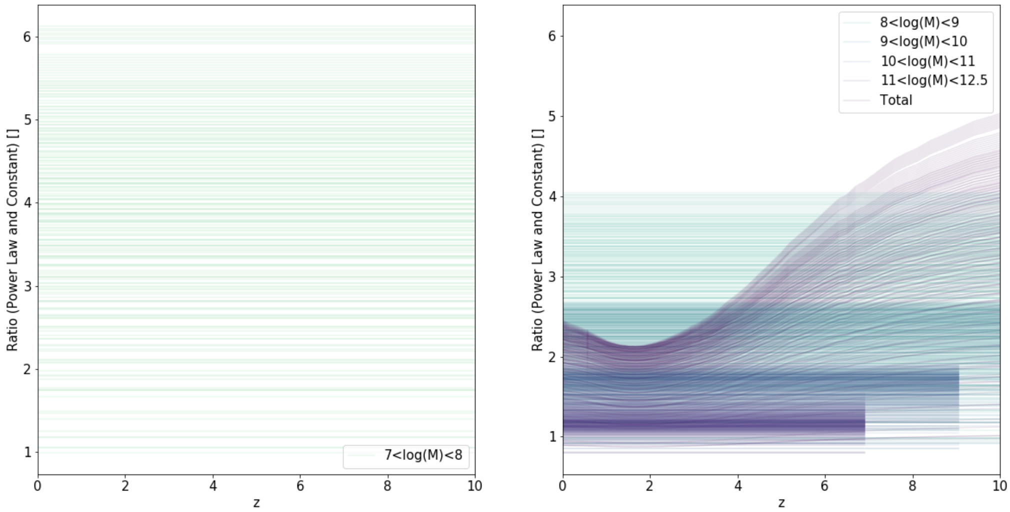

Figure 26: Ratio of the rate from the power law models to the constant model for the $10^7 - 10^8 M_\odot$ mass bin (*left panel*) and the other five mass bins and the total rate (*right panel*).

The results in this thesis suggest a SNe IIn preference for low mass galaxies. However, as mentioned in Section 3.1.3, other similar studies do not agree on this matter. But we know that SLSNe are more common in low mass galaxies compared to regular CC SNe. One of the SNe IIn in Graur et al. (2017b) is significantly brighter than the rest as can be seen in Table 1 in Section 4.1, so could this SN drive the host galaxy mass dependence that is seen in Figure 16? Since we are only working with five SNe IIn in this case, only one of them could perhaps affect the results significantly, but then again uncertainties have a huge impact for such a small data set, and this could be the reason for the low mass host preference. A larger number of both SNe IIn and SLSNe-IIn is needed to explore this possibility further.

6.1 Lensing

Now that the IIn rates have been calculated for all of the IIn/CC power law models, the final goal is to find out how these rates would change the estimated annual number of lensed IIn's from LSST and subsequently make a comparison with the results from Wojtak et al. (2019). The aim is obtain estimations for the bands g, r, i, z and y and therefore, the expected limiting magnitudes for LSST are needed. According to Table 3 in the Baseline Operations Simulation from LSST revised in 2018 (also known as baseline2018a[1]), the expected limiting magnitudes are 24.47 in g, 24.07 in r, 23.54 in i, 22.72 in z and 21.82 in y. To estimate the annual number of lensed IIn for LSST, we use the simulation pipeline from Wojtak et al. (2019), which is not publicly available. The simulation is based on a Monte Carlo approach and generates a sample of lens galaxies and SNe within a light cone, then calculates the lensing properties and applies detection criteria (as mentioned in Section 3.3.2) in order to estimate the number of lensed SNe of different types. For more details on the simulation, we refer the reader to Wojtak et al. (2019). For our analysis, the simulation is run using the rates based on a R(IIn/CC) of 0.034. The code is also run for each band using the corresponding limiting magnitude.

From the simulations, we need the supernova redshifts and corresponding weights for each band for the constant rate model to plot as a histogram using the redshift values from earlier results. To obtain the numbers for the power law models, first the ratios between the power law models and the constant or reference model is calculated and any NaN (undefined) values are set to zero. The ratios are then multiplied by the histogram values for each band. The results are almost ready, but the redshift bins are not all of the same width, which means that comparing them directly makes no sense. In order to circumvent this problem, we use the relative frequency density:

$$\text{relative frequency density} = \frac{\text{frequency}}{\text{bin width} \cdot N_{data}}, \tag{27}$$

where N_{data} is the number of data items. This method allows a meaningful comparison of the bins when they are not equally spaced.

The final step is to smooth the data to get rid of the noise impact by introducing a Savitzky-Golay filter. This method is based on a local least-squares polynomial approximation, which means that successive subsets of a certain window-length of the data are fitted by a low-order polynomial to smooth out the noise effects. For more details, see Savitzky & Golay (1964). For g, r and i bands, a window-length of 25 and a second order polynomial is used. For z and y, window-lengths of 35 and 45 are employed, respectively. The results are plotted in Figure 27. It is clear from the plot that it is more likely to observe lensed IIn in the g-band since they are brighter in the bluer bands. Constant models using a R(IIn/CC) of 0.05 and 0.034 are both shown in this plot. This is in the interest of directly comparing the lensed IIn yield of Wojtak et al. (2019) to the results from the power law models. Note that Figure 27 refers to all of the lensed SNe IIn

[1] https://docushare.lsst.org/docushare/dsweb/Get/Version-52280/Doc-28453.pdf

out to redshift 3 for the whole sky according to the simulation. These cannot all be detected by our surveys and telescopes, so one needs to make quite a few assumptions in order to come up with a practical estimate of the number of lensed SNe from a survey. First of all, LSST will cover about half of the sky, such that we will have no chance of observing so many of these simulated lensed SNe IIn. Some of the other assumptions behind the LSST estimations from Wojtak et al. (2019) emanate from the detection methods as mentioned in Section 3.3.3. For the magnification method, the observed possibly lensed SN should be brighter than what is expected for a SNe IIn by a significant amount. Unfortunately, SNe IIn have very diverse light curves and so it is not so easy to define a standard SN IIn. For multiple imaging, the images should be bright enough for detection, but should not be so close that they blend together, which is difficult to achieve for many lensed SNe with the current and near-future instruments available. In addition, a general underlying assumption about the luminosity function of the SNe in the simulation influences the outcome. Because of all of these contributions to the uncertainty of the estimated numbers of lensed SNe IIn in Wojtak et al. (2019), we have chosen to not compare with the estimatd number of lensed SNe IIn, but instead the total theoretically predicted number.

Figure 27 shows that LSST will not observe any lensed SNe IIn beyond redshift 3, as these will be too faint. As even the most extreme models exhibit no effect of the low mass bias for SNe IIn on the rate below redshift 4, LSST estimated lensed SNe IIn will not be affected by this. But in Section 4.1.1, it is noted that Graur et al. (2017b) mention the low-luminosity galaxy incompleteness of the LOSS sample and argue that this will not have an effect on the results in their work. However, when using the available data to compare the rates of different SN types between low and high mass galaxies, one would expect that galaxy incompleteness has an influence on the results. The resulting factor of lensed SNe IIn predicted in this thesis would probably have been higher if the LOSS galaxy sample was complete with respect to luminosity, and so one can argue that the SNe IIn bias with respect to low mass host galaxies is still underestimated when it comes to the underlying galaxy sample.

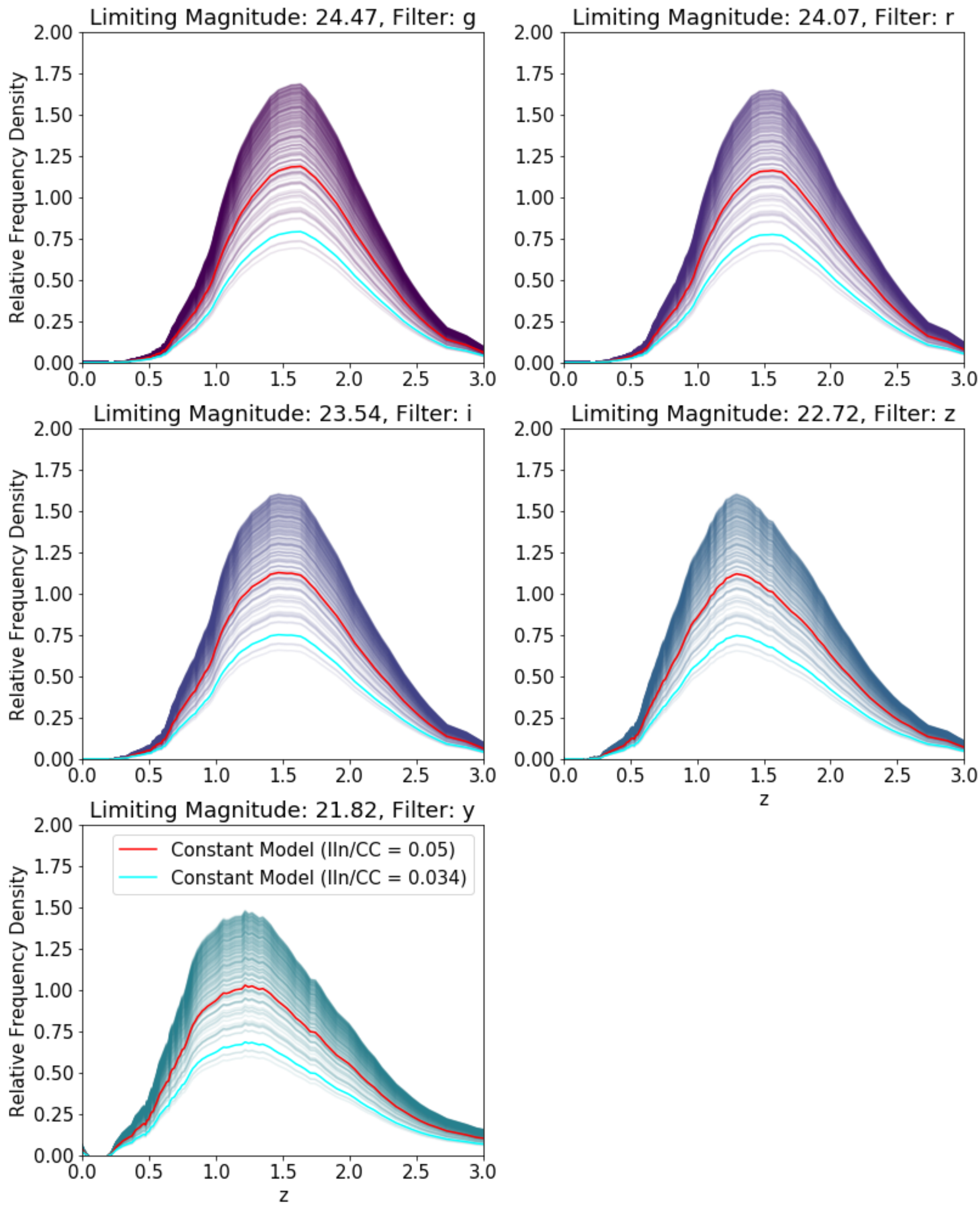

Figure 27: Relative frequency density of lensed IIn vs redshift for the 207 power law models compared to a constant model using R(IIn/CC) of 0.05 as in Wojtak et al. (2019).

7 Conclusion

It has been estimated that SNe IIn will dominate in lensed SN surveys like the upcoming LSST. Predictions from Wojtak et al. (2019) and others estimate the number of lensed IIn from LSST at around 200 per year assuming a constant IIn to CC ratio of 0.05. This ratio can instead be modelled as a power law based on SN data from LOSS, revealing a possible bias towards low mass galaxies for this SN type. Not all studies find this low mass host galaxy preference for regular SNe IIn though, while there seems to be a clear deficit of massive host galaxies for the SLSNe-IIn. It is unclear whether the bright SNe IIn 2010jl is driving the low mass host galaxy bias for SNe IIn in the LOSS data set.

The local IIn to CC ratio has been quoted as 0.05 (Wojtak et al., 2019; Graur et al., 2017b)) and 0.09 (Li et al., 2011a). However, when using all constraints from the LOSS data and requiring a constant solution, the ratio becomes 0.034 ± 0.009.

The subsequently calculated volumetric SNe IIn rate shows a higher rate for the power law models for a redshift greater than 4. The contribution from the less massive host galaxies increases in this area. The results also indicate an overall higher rate for most power law models compared to the constant model. However, the power law models were not weighted with the SFR and consequently the SMF during the model selection. This means that the more massive galaxies dominate the results and perhaps this is also the source of the skewed distribution of the power law solutions. This requires further research.

The estimations of lensed SNe IIn from LSST from Wojtak et al. (2019) are not affected by the increased contribution from the less massive host galaxies, as this effect only occurs at redshift 4 and above. LSST will not be able to detect lensed SNe further than redshift 3 as the sources become too faint for the survey. However, implementing the SMF weighting will change the outcome of the model selection and potentially change this result.

8 Future Work

The work in this thesis is still ongoing and many questions remain to be answered. First of all, it will be interesting to see the effect of weighting the constraints with the stellar mass function. In such a framework, the distribution of host galaxy masses will be taken into account and possibly sort out the asymmetry of the solution distribution.

Since the results in this thesis are based on only around five IIns and around 100 CC SNe from LOSS, it would be a clear improvement to work with a larger data set. The Palomar Transient Factory (PTF) CC SN and host galaxy sample is presented in Schulze et al. (2020), containing 111 regular type IIn SNe and 16 SLSNe-IIn. This sample could be a good choice for the analysis of the IIn to CC ratio to investigate if the bias towards low stellar mass galaxies for the LOSS sample can be reproduced with PTF data. It would be interesting to also study the SLSNe-IIn and their preference for low mass host galaxies as well. The distribution of the CC SN types in the PTF sample can be seen in Figure 28.

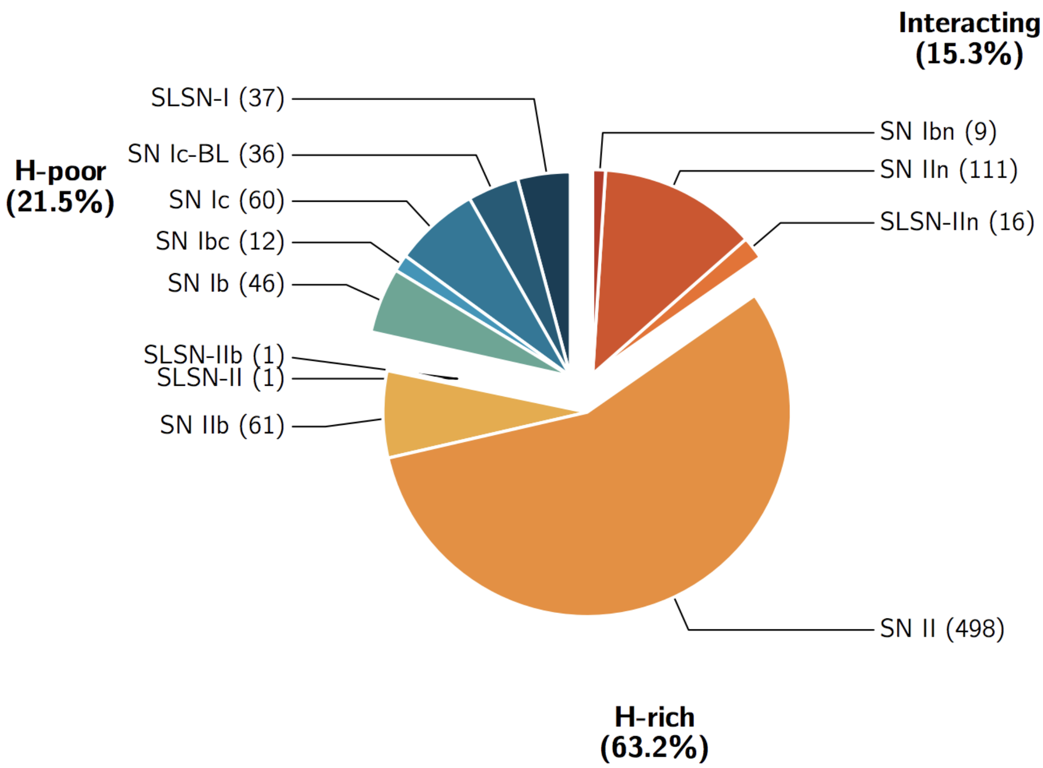

Figure 28: Distribution of the CC SN types in the PTF sample. Figure is from Schulze et al. (2020).

The same analysis could be carried out for other CC SN types from the PTF sample. From the SN rates computed in Frohmaier et al. (2021), as illustrated in Figure 29, the general rate of all

CC SNe seems to decrease with host galaxy mass, indicating the same trend for IIn as that found by Graur et al. (2017b). It could be that the ratio of a specific type to all CC will not be constant as a function of redshift no matter what subtype, which is worth investigating.

Another aspect that has not been discussed in this thesis is the rate of type Ia SNe. It would be very useful to investigate the rate of this type because these are particularly interesting in the cosmological context.

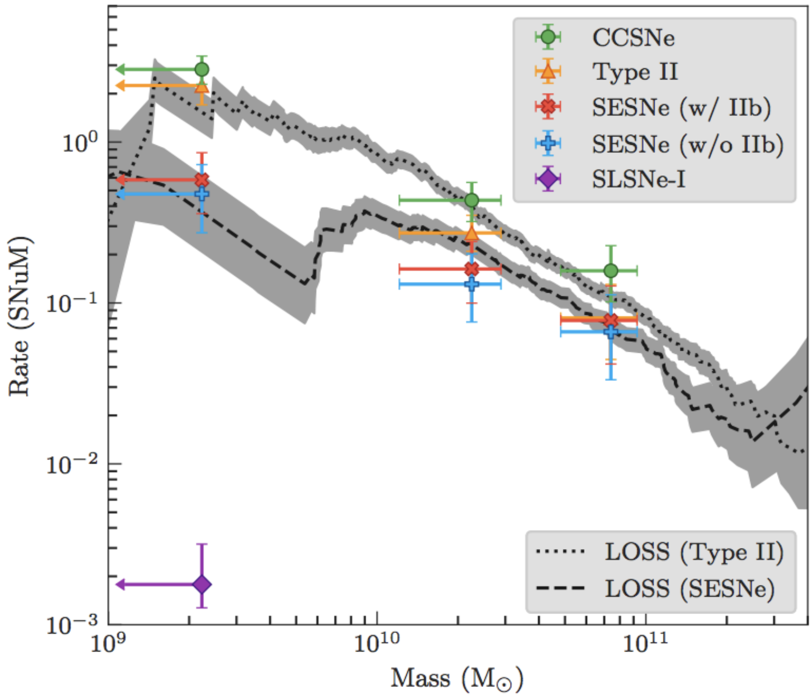

Figure 29: SN rates as a function of host galaxy stellar mass compared to rates from LOSS. Figure is from Frohmaier et al. (2021).

Also potentially exploring the effects for other upcoming surveys and instruments could be of interest. Like the Nancy Grace Roman Space Telescope (AKA Roman Space Telescope). According to Pierel et al. (2021) the redshift range is up to 4 (See Figure 30) for this mission and so there is a potential to see an effect of the low mass host galaxy bias for SNe IIn observed in this work, which should start to affect any results at around redshift 4.

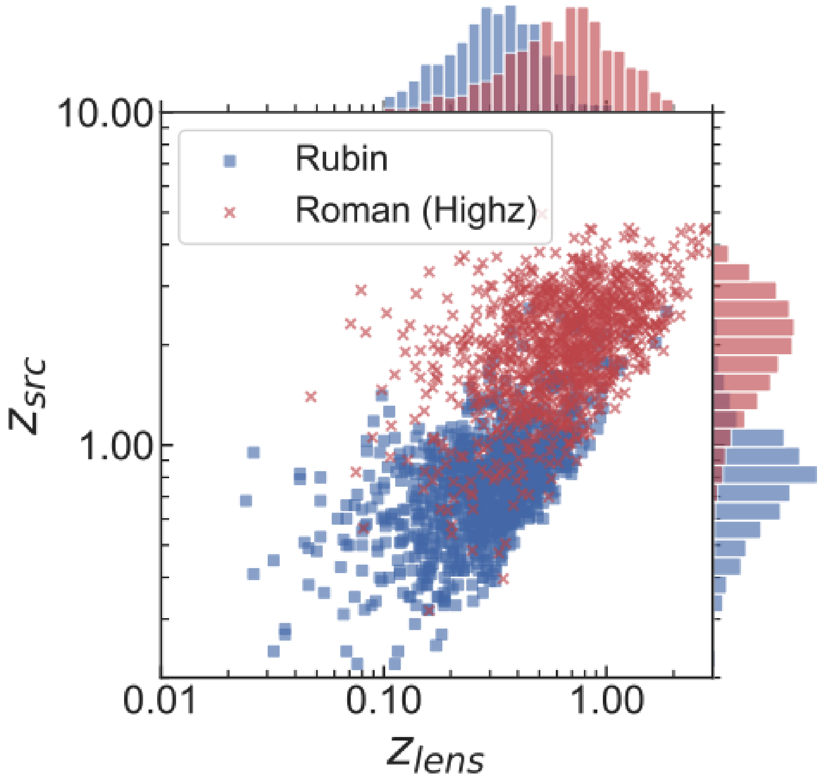

Figure 30: Redshift of sources versus redshift of lenses comparing LSST (Rubin) and Roman Space Telescope. Figure is from Pierel et al. (2021).

9 Acknowledgements

Thank you to my supervisor Jens Hjorth for always believing in me and being there to answer all of my questions, however basic they may be. Thank you to Radoslaw Wojtak for sharing his insight and giving me access to the simulation behind his results. Thank you to Christa Gall and Doogesh Kodi Ramanah for reading through all of the words that make up this thesis. Also thank you to Jo Verwohlt Damm, Nikki Arendse and Sophie Schrøder for great advice and for providing much needed moral support through the final stages of the project.

References

Ade P. A. R., et al., 2016, Astronomy & Astrophysics, 594, A13

Angus C. R., Levan A. J., Perley D. A., Tanvir N. R., Lyman J. D., Stanway E. R., Fruchter A. S., 2016, MNRAS, 458, 84

Arcavi I., 2017, Hydrogen-Rich Core-Collapse Supernovae. p. 239, doi:10.1007/978-3-319-21846-5˙39

Barbon R., 1968, AJ, 73, 1016

Behroozi P. S., Wechsler R. H., Conroy C., 2013, ApJ, 770, 57

Behroozi P., Wechsler R. H., Hearin A. P., Conroy C., 2019, MNRAS, 488, 3143

Bevan A., et al., 2019, in Supernova Remnants: An Odyssey in Space after Stellar Death II. p. 142

Bilinski C., Smith N., Li W., Williams G. G., Zheng W., Filippenko A. V., 2015, MNRAS, 450, 246

Bonvin V., et al., 2017, MNRAS, 465, 4914

Chabrier G., 2003, PASP, 115, 763

Foley R. J., Smith N., Ganeshalingam M., Li W., Chornock R., Filippenko A. V., 2007, ApJ, 657, L105

Frohmaier C., et al., 2021, MNRAS, 500, 5142

Gal-Yam A., 2019, ARA&A, 57, 305

Gall C., et al., 2014, Nature, 511, 326

Gao Y., et al., 2018, ApJ, 869, 15

Goldstein D. A., Nugent P. E., 2017, ApJ, 834, L5

Goldstein D. A., Nugent P. E., Goobar A., 2019, ApJS, 243, 6

Grassitelli L., Langer N., Mackey J., Graefener G., Grin N., Sander A., Vink J., 2020, arXiv e-prints, p. arXiv:2012.00023

Graur O., Bianco F. B., Modjaz M., 2015, Monthly Notices of the Royal Astronomical Society, 450, 905–925

Graur O., Bianco F. B., Huang S., Modjaz M., Shivvers I., Filippenko A. V., Li W., Eldridge J. J., 2017a, ApJ, 837, 120

Graur O., Bianco F. B., Modjaz M., Shivvers I., Filippenko A. V., Li W., Smith N., 2017b, ApJ, 837, 121

Grillo C., et al., 2018, ApJ, 860, 94

Hopkins A. M., 2018, PASA, 35, e039

Kelly P. L., Kirshner R. P., 2012, ApJ, 759, 107

Kelly P. L., et al., 2015, Science, 347, 1123

Kroupa P., 2001, MNRAS, 322, 231

Larson R. B., 1998, MNRAS, 301, 569

Leaman J., Li W., Chornock R., Filippenko A. V., 2011, MNRAS, 412, 1419

Li W. D., 2000, AIP Conference Proceedings

Li W., et al., 2011a, MNRAS, 412, 1441

Li W., Chornock R., Leaman J., Filippenko A. V., Poznanski D., Wang X., Ganeshalingam M., Mannucci F., 2011b, MNRAS, 412, 1473

Linder E. V., 2011, Phys. Rev. D, 84, 123529

Madau P., Dickinson M., 2014, ARA&A, 52, 415

Maguire K., 2017, Type Ia Supernovae. p. 293, doi:10.1007/978-3-319-21846-5˙36

Mauerhan J. C., et al., 2013, MNRAS, 431, 2599

Meng X., Gao Y., Han Z., 2017, SNe Ia as a cosmological probe. pp 151–172, doi:10.1142/9789814678506˙0004

Moriya T. J., Sorokina E. I., Chevalier R. A., 2018, Space Sci. Rev., 214, 59

Neill J. D., et al., 2011, ApJ, 727, 15

Nyholm A., et al., 2020, A&A, 637, A73

Pierel J. D. R., Rodney S., 2019, ApJ, 876, 107

Pierel J. D. R., Rodney S., Vernardos G., Oguri M., Kessler R., Anguita T., 2021, ApJ, 908, 190

Planck Collaboration et al., 2018, preprint, (arXiv:1807.06209)

Quimby R. M., et al., 2018, ApJ, 855, 2

Refsdal S., 1964, MNRAS, 128, 307

Riess A. G., Casertano S., Yuan W., Bowers J. B., Macri L., Zinn J. C., Scolnic D., 2021, ApJ, 908, L6

Salpeter E. E., 1955, ApJ, 121, 161

Sanders N. E., et al., 2015, VizieR Online Data Catalog, p. J/ApJ/799/208

Savitzky A., Golay M. J. E., 1964, Analytical Chemistry, 36, 1627

Schulze S., et al., 2018, MNRAS, 473, 1258

Schulze S., et al., 2020, arXiv e-prints, p. arXiv:2008.05988

Shimizu I., Inoue A. K., 2013, Publications of the Astronomical Society of Japan, 65, 96

Smith N., 2017, Interacting Supernovae: Types IIn and Ibn. p. 403, doi:10.1007/978-3-319-21846-5˙38

Stritzinger M., et al., 2012, ApJ, 756, 173

Strolger L.-G., et al., 2015, ApJ, 813, 93

Vega-Ferrero J., Diego J. M., Miranda V., Bernstein G. M., 2018, ApJ, 853, L31

Wechsler R. H., Tinker J. L., 2018, Annual Review of Astronomy and Astrophysics, 56, 435–487

Wojtak R., Hjorth J., Gall C., 2019, MNRAS, 487, 3342